Controlling the alignment of rodlike colloidal particles with time-dependent shear flows

Brian D. Leahy, Donald L. Koch, and Itai Cohen

Citation: Journal of Rheology **61**, 979 (2017); doi: 10.1122/1.4996009
View online: http://dx.doi.org/10.1122/1.4996009
View Table of Contents: http://sor.scitation.org/toc/jor/61/5
Published by the The Society of Rheology

Controlling the alignment of rodlike colloidal particles with time-dependent shear flows

Brian D. Leahy

Department of Physics, Cornell University, Ithaca, New York 14853

Donald L. Koch

Chemical and Biomolecular Engineering, Cornell University, Cambridge, UK

Itai Cohen

Department of Physics, Cornell University, Cambridge, UK

(Received 19 December 2016; final revision received 28 June 2017; published 4 August 2017)

Abstract

While colloidal suspensions of nonspherical particles have been studied for decades, most work has focused on describing their behavior in flows with simple time behavior. Little is known about their behavior in flows with complex variations in time, and in particular, the possibility of varying the flow to control the suspension's properties. Here, we take advantage of a recent solution for the orientation dynamics of a dilute suspension under an *arbitrary* periodic, high-frequency shear flow to control particle alignment and suspension rheology. Working in the twin limit of rapid oscillations ($\mathrm{Pe} = 1/DT_{cyc} \gg 1$, where D is the rotary diffusivity and T_{cyc} is the oscillation period) and long times t ($Dt \gg 1$), we use a periodic simple shear waveform to strongly align particle orientations, aligning the orientations more strongly than steady shear by a factor proportional to the particle aspect ratio. Since particle orientations couple to the suspension stress, we can strongly control the rheology, maximizing and minimizing the viscosity and creating large normal stress signals. Surprisingly, the optimal waveforms are extremely simple, providing an intuitive understanding of the mechanisms for controlling particle alignment and suspension rheology. *© 2017 The Society of Rheology.*
[http://dx.doi.org/10.1122/1.4996009]

I. INTRODUCTION

The interplay between an applied flow and particle orientation creates a diverse set of behaviors in suspensions of elongated particles. The particles' additional orientational degree of freedom couples to the applied flow. The flow rotates the particle orientations, and the orientations in turn affect the suspension's stress. As a result, suspensions of anisotropic particles display a rich set of non-Newtonian rheological behaviors, even in the dilute limit in simple flows. However, the difficulty of solving the underlying equations of motion has prevented analysis of the dynamics of anisotropic particle suspensions except in the most basic flow fields, such as steady simple shear or extensional flows. Extending this understanding to more complicated flows could allow for new control over the suspension properties, such as strongly aligning particle orientations or minimizing the suspension's viscosity.

Jeffery [1] was the first to investigate suspensions of ellipsoidal particles under simple shear. He found that these particles rotate in an unsteady motion known as a Jeffery orbit. For a spheroidal particle of aspect ratio r in a simple shear flow, the particle's unit normal $\boldsymbol{p}(\theta, \phi)$ evolves with time t as

$$\begin{aligned} \tan\phi &= r\tan\left(\frac{\Gamma(t)}{r+1/r} + \kappa\right) \\ \tan\theta &= C\left(r\cos^2\phi + \frac{1}{r}\sin^2\phi\right)^{-1/2}, \end{aligned} \tag{1}$$

where $\Gamma(t)$ is the accumulated shear strain of the applied flow, and the phase angle κ and orbit constant C are constants of integration. The particle's orientation $\boldsymbol{p}(\theta, \phi)$ is parameterized by the polar angle from the vorticity direction θ and the azimuthal angle from the gradient direction ϕ. For most particles [2], the rotation is periodic, and the Jeffery orbit only advects the initial distribution of particle orientations. Additional effects other than the Jeffery orbit are required to create a unique long-time distribution.

In colloidal suspensions, rotational diffusion randomizes the particle orientations. In a shear flow, both the deterministic Jeffery orbits and the random rotational diffusion determine the final orientation distribution ρ, as described by a Fokker-Planck equation in orientation space

$$\frac{\partial\rho}{\partial t} = D\nabla^2\rho - \boldsymbol{\nabla}\cdot(\rho\boldsymbol{\omega}), \tag{2}$$

where D is the rotational diffusivity. For dilute suspensions in a time-varying simple shear flow, the rotational velocity $\boldsymbol{\omega}$

is the Jeffery orbit rotational velocity. Either Jeffery's solution or symmetry considerations [3] give this rotational velocity as

$$\begin{aligned}\boldsymbol{\omega} &= \boldsymbol{p}\cdot\boldsymbol{\Omega} + \frac{r^2-1}{r^2+1}[\boldsymbol{E}\cdot\boldsymbol{p} - \boldsymbol{p}(\boldsymbol{p}\cdot\boldsymbol{E}\cdot\boldsymbol{p})] \\ &= \hat{\boldsymbol{\phi}}\,\frac{\dot{\gamma}(t)}{r+1/r}\left(r\cos^2\phi + \frac{1}{r}\sin^2\phi\right)\sin\theta \\ &\quad + \hat{\boldsymbol{\theta}}\,\frac{\dot{\gamma}(t)(r^2-1)}{4(r^2+1)}\sin 2\phi\sin 2\theta, \end{aligned} \tag{3}$$

where $\Omega = (\nabla \boldsymbol{v} - \nabla \boldsymbol{v}^T)/2$ and $\boldsymbol{E} = (\nabla \boldsymbol{v} + \nabla \boldsymbol{v}^T)/2$ are the instantaneous vorticity and rate-of-strain tensors, ˆ and $\hat{\phi}$ are unit vectors along the θ and ϕ directions, and $\dot{\gamma}(t)$ is the instantaneous strain rate of the flow. The combined effects of diffusion and Jeffery orbits produce an interesting array of orientation distributions and suspension rheology that are fairly well understood for steady shear at long times. The Péclet number Pe, the ratio of the flow's shear rate to the particle's rotational diffusivity, determines the relative importance of diffusion versus particle reorientation by the Jeffery orbit. At low Pe, diffusion dominates and results in an isotropic orientation distribution and a high suspension viscosity [4,5]. To first order in Pe, the flow creates a slight alignment along the extensional axis, but the suspension viscosity remains the same. Conversely, at high Pe, diffusion causes a randomization of the rod's orientations only insofar as to result in a distribution that does not change in time [6]. Particles tend to align fairly strongly with the flow, where the Jeffery orbit is slowest, which also results in a relatively low suspension viscosity. There is a third regime at intermediate Pe such that $1 \ll \mathrm{Pe} \ll (r^3 + r^{-3})$, where the Jeffery orbit is dominant over diffusion almost everywhere except in a small region near the flow direction where diffusion dominates [7]. In this regime, the particles align near the flow direction, but not as strongly as they do in the high-Pe regime.

While extensive research has focused on describing steady shear of axisymmetric particle suspensions, much less work has focused on describing their behavior in time-varying flows [8]. The time-dependent convection-diffusion equations for rod orientation dynamics are extremely complicated to solve even in the dilute limit; as yet there is not a complete solution even for the startup of steady shear. As a result, an engineer who desires to control a suspension of axisymmetric particles through shear is essentially limited to either exploring long-time steady shear at various Pe or to experimenting through trial-and-error. In this paper, we take the first steps toward creating a theory for *controlling* the flow behavior of suspensions of axisymmetric particles. We take advantage of a recent analytical solution to the orientation dynamics of axisymmetric particles under an *arbitrary* periodic shear flow, albeit for particles confined to the flow-gradient plane at high Pe [9]. We use this exact solution to optimize desired properties of the suspensions such as maximizing particle alignment, maximizing and minimizing the suspension shear viscosity, and maximizing the normal stress difference. Our results are valid at short oscillation periods ($\mathrm{Pe} \equiv 1/DT_{cyc}$) and after initial transients have decayed ($Dt \gg 1$). Surprisingly, the optimal waveforms for controlling suspension behavior are extremely simple and allow for a precise intuition for the mechanism for controlling suspension properties. Along with previous similarities between the restricted and full orientation dynamics [9,10], this intuition suggests that the results and qualitative features of the optimal waveforms will carry over to real suspensions of particles that can rotate freely in three dimensions.

II. ORIENTATIONS CONFINED TO THE FLOW-GRADIENT PLANE

For particles confined to the flow-gradient plane, the complicated advection-diffusion equation (2) in orientation space simplifies to

$$\begin{aligned}\frac{\partial\rho}{\partial t} &= D\frac{\partial^2\rho}{\partial\phi^2} - \frac{\partial}{\partial\phi}\left[\dot{\Gamma}(t)\omega(\phi)\rho\right], \\ \omega(\phi) &= \frac{1}{r+1/r}\left(r\cos^2\phi + \frac{1}{r}\sin^2\phi\right), \end{aligned} \tag{4}$$

where $\dot{\Gamma}(t)$ is the instantaneous strain rate of the applied flow and $\omega(\phi)$ is the rotational velocity per unit strain rate. At high Pe the distribution $\rho(\phi, t)$ changes with time in an exceptionally complicated manner [9]. The nonuniform velocity of the Jeffery orbit compresses and expands $\rho(\phi, t)$ and rotates these inhomogeneities with the orbit. These distortions occur on two fast timescales—a flow timescale $\sim 1/\dot{\Gamma}$ and an oscillation timescale associated with time variations in $\dot{\Gamma}(t)$. Diffusion then relaxes the distribution on an additional, diffusive timescale $\sim 1/D$ that is much slower than the flow and oscillation timescales. The distribution does not necessarily relax to a steady state, but may continue to change with the flow's oscillations. At high Pe, $\rho(\phi, t)$ changes rapidly with time because a particle's phase angle κ and orbit constant C in Eq. (1) are roughly constant with time, while its orientation ϕ changes rapidly with time due to the Jeffery orbit.

As a result, at high Pe the orientation dynamics are much simpler when described in terms of the distribution of the particles' phase angles $f(\kappa)$ instead of the distribution of their orientations $\rho(\phi)$ [9,11]. These two distributions are related by $f(\kappa)\,d\kappa = \rho(\phi)\,d\phi$; the coordinate relationship between κ and ϕ defined by the Jeffery orbit in Eq. (1) gives [9]

$$\begin{aligned}\rho &= \frac{\bar{\varpi}}{\omega(\phi)}f(\kappa) \\ &= \frac{1}{r\cos^2\phi + 1/r\sin^2\phi} \times f(\kappa) \\ &= \left[1/r\cos^2(\kappa + \bar{\varpi}\Gamma(t)) + r\sin^2(\kappa + \bar{\varpi}\Gamma(t))\right] \times f(\kappa), \end{aligned} \tag{5}$$

where $\bar{\varpi} = 1/(r + 1/r)$ is the average particle rotation per unit strain. When $D = 0$, the distribution of phase angles $f(\kappa)$ remains constant with time, as the particles only reorient due to their Jeffery orbits. In contrast, the orientation distribution $\rho(\phi)$ changes rapidly, as the Jeffery orbit stretches and advects the distribution. Likewise, when the rotational diffusion is nonzero but weak, the particle orientations are described much more simply in terms of $f(\kappa)$ than $\rho(\phi)$. By construction, $f(\kappa)$ evolves only due to diffusion, changing only on the long time scale $\sim 1/D$. For an arbitrary periodic strain waveform $\Gamma(t)$, the phase-angle distribution $f(\kappa)$ evolves as [9]

$$\frac{\partial f}{\partial t} = -\frac{\partial}{\partial \kappa}\left[-\mathfrak{D}(\kappa)\frac{\partial f}{\partial \kappa} - \frac{1}{2}\frac{\partial \mathfrak{D}}{\partial \kappa} f\right] \tag{6}$$

in the limit that the characteristic diffusion time is large compared to the period of the waveform T_{cyc}: $\mathrm{Pe} \equiv 1/DT_{cyc} \gg 1$. Here, $\mathfrak{D}(\kappa)$ is an effective phase-angle dependent rotational diffusion, defined through the inverse-square of the particle's rotational velocity time-averaged over a cycle

$$\begin{aligned}\mathfrak{D}(\kappa)/D &= \frac{1}{T_{cyc}}\int_0^{T_{cyc}}\left(\frac{\bar{\omega}}{\omega(\kappa+\bar{\omega}\Gamma(t))}\right)^2 dt\\ &= \frac{1}{T_{cyc}}\int_0^{T_{cyc}}\left[\frac{1}{r}\cos^2\left(\kappa+\frac{\Gamma(t)}{r+1/r}\right)\right.\\ &\quad\left. + r\sin^2\left(\kappa+\frac{\Gamma(t)}{r+1/r}\right)\right]^2 dt.\end{aligned} \tag{7}$$

In particular, at long times $Dt \gg 1$ $f(\kappa)$ has a simple steady-state solution that does not change with time

$$f(\kappa) \propto (\mathfrak{D}(\kappa)/D)^{-1/2}, \tag{8}$$

regardless of how complicated the applied shear flow is. In contrast, even for $Dt \gg 1$ the orientation distribution $\rho(\phi, t)$ changes rapidly in t for flows with all but the simplest time dependencies. Physically, the orientation distribution is determined through diffusion by a memory of the average applied shear flow through $\mathfrak{D}(\kappa)$. The particles migrate to regions of low phase-angle diffusivity, as is common in systems ranging from the creation of concentration gradients in turbophoresis [12,13] to absorbing states in dense, non-Brownian suspensions [14,15]. The memory of the applied flow is only determined by time-averages of functions of the shear strain, independent of the strain rate, the frequency of the oscillation, and the orders in which the strains occurred. The particle orientations forget their initial conditions on an enhanced time scale $\propto 1/D$ [9].

Figure 1 illustrates these two distinct ways of viewing the evolution of particle orientations with time. Under steady shear, a steady-state solution for ρ exists, as shown in Fig. 1(a) for a suspension of particles with $r = 5.0$. The distribution is symmetric with respect to inverting the particle's orientation ($\boldsymbol{p} \to -\boldsymbol{p}$ or $\phi \to \phi + \pi$), keeping the symmetry of the Jeffery orbit. As $\mathrm{Pe} \to \infty$, the steady-state solution corresponds to an orientation distribution $\rho(\phi)$ that is inversely proportional to $\omega(\phi)$. The orientation distribution $\rho(\phi)$ is suppressed by $\propto 1/r$ near the gradient direction (at $\phi = 0$ and π), where the particles rotate rapidly, and is enhanced by $\propto r$ along the flow direction (at $\phi = \pi/2$ and $3\pi/2$), where particles rotate slowly. In contrast, in κ-space the distribution $f(\kappa)$ is constant, as diffusion effectively erases the memory of the starting time of the shear [panel (b)]. Translating from $f(\kappa)$ to $\rho(\phi)$ involves multiplying by the prefactor $\bar{\omega}/\omega(\phi)$ in Eq. (5). Since $\phi = \phi(\kappa + \bar{\omega}\Gamma(t))$ [cf. Eq. (1)] and since $\Gamma(t) = \dot{\gamma}t$ for steady shear, this prefactor $\bar{\omega}/\omega$ translates with a fixed velocity in κ space, as illustrated by the lower portion of panel b.

Under oscillatory shear, the long-time distributions are considerably simpler when described in terms of $f(\kappa)$ than when described in terms of $\rho(\phi)$. As the flow oscillates, the orientation distribution $\rho(\phi, t)$ does not approach a steady-state value but is stretched and rotated with the flow in a complicated manner throughout each cycle, as indicated in Fig. 1(c). For the sinusoidal shear with strain amplitude 1 shown in the figure, at the center of the cycle the distribution is almost isotropic, but is slightly distorted. As the suspension is sheared, the distribution is first stretched along the extensional axis by the term $\propto \boldsymbol{E}\cdot\boldsymbol{p} - \boldsymbol{p}(\boldsymbol{p}\cdot\boldsymbol{E}\cdot\boldsymbol{p})$ in Eq. (3), then rotated by the flow to be more closely aligned along the flow axis ($\Gamma(t) = 1$ curve). Reversing the flow first returns the distribution to its value at the center of the cycle before repeating the stretching and rotation in the opposite direction.

In contrast, at high Pe this picture is much simpler in terms of the phase-angle distribution $f(\kappa)$. The phase-angle distribution .. attains a steady-state form that is constant in time [upper portion of panel (d)] and is determined solely by $\mathfrak{D}(\kappa)$ through Eqs. (7) and (8). For the moderate strain amplitude shown in panel d, $\bar{\omega}\Gamma$ is small, and $\mathfrak{D}(\kappa) \approx (\bar{\omega}/\omega(\kappa))^2$. Thus, $\mathfrak{D}(\kappa)$ is small in regions where the Jeffery orbit velocity is small, and vice versa. Since $f(\kappa) \propto 1/\sqrt{\mathfrak{D}(\kappa)}$, in Fig. 1(d) $f(\kappa)$ is enhanced at phase angles corresponding to particles that rotate rapidly with the Jeffery orbit (near $\kappa = 0, \pi$), and is suppressed at phase angles corresponding to particles that rotate slowly with the Jeffery orbit (near $\kappa = \pi/2, 3\pi/2$). This $f(\kappa)$, in conjunction with the initial centering of the trough in $\bar{\omega}/\omega$ about the peak in $f(\kappa)$, corresponds to the initially mostly isotropic distribution $\rho(\phi)$. The stretching and rotation of $\rho(\phi)$ with time simply corresponds to the oscillation of the prefactor $\bar{\omega}/\omega$ about the peak in $f(\kappa)$. As the trough in $\bar{\omega}/\omega$ shifts slightly to either side of the peak in $f(\kappa)$, the overlap between $f(\kappa)$ and $\bar{\omega}/\omega$ increases and $\rho(\phi)$ becomes more strongly peaked.

Motivated by the simple description for orientation dynamics at high Pe, we proceed to optimize the orientation distribution for a desired property. Equations (5), (7), and (8) completely determine the steady-state orientation distributions at long-times for an *arbitrary* shear waveform. Moreover, while in practice $\mathfrak{D}(\kappa)$ may be difficult to calculate analytically, it is extremely simple to calculate numerically—as we will show, two quadratures determine $\mathfrak{D}(\kappa)$, which in turn determines the form of $f(\kappa)$ aside from a normalization constant. As a result, we can simply parameterize an arbitrary waveform and fit these parameters to optimize any desired property determined by the orientation distribution.

III. MAXIMIZING ALIGNMENT

Strongly aligned particle orientations are crucial for engineering applications of nonspherical particle suspensions. For instance, a well-defined orientation strongly affects the mechanical stiffness [16] and thermal or electrical conductivity [17–19] of a fiber-reinforced composite, and

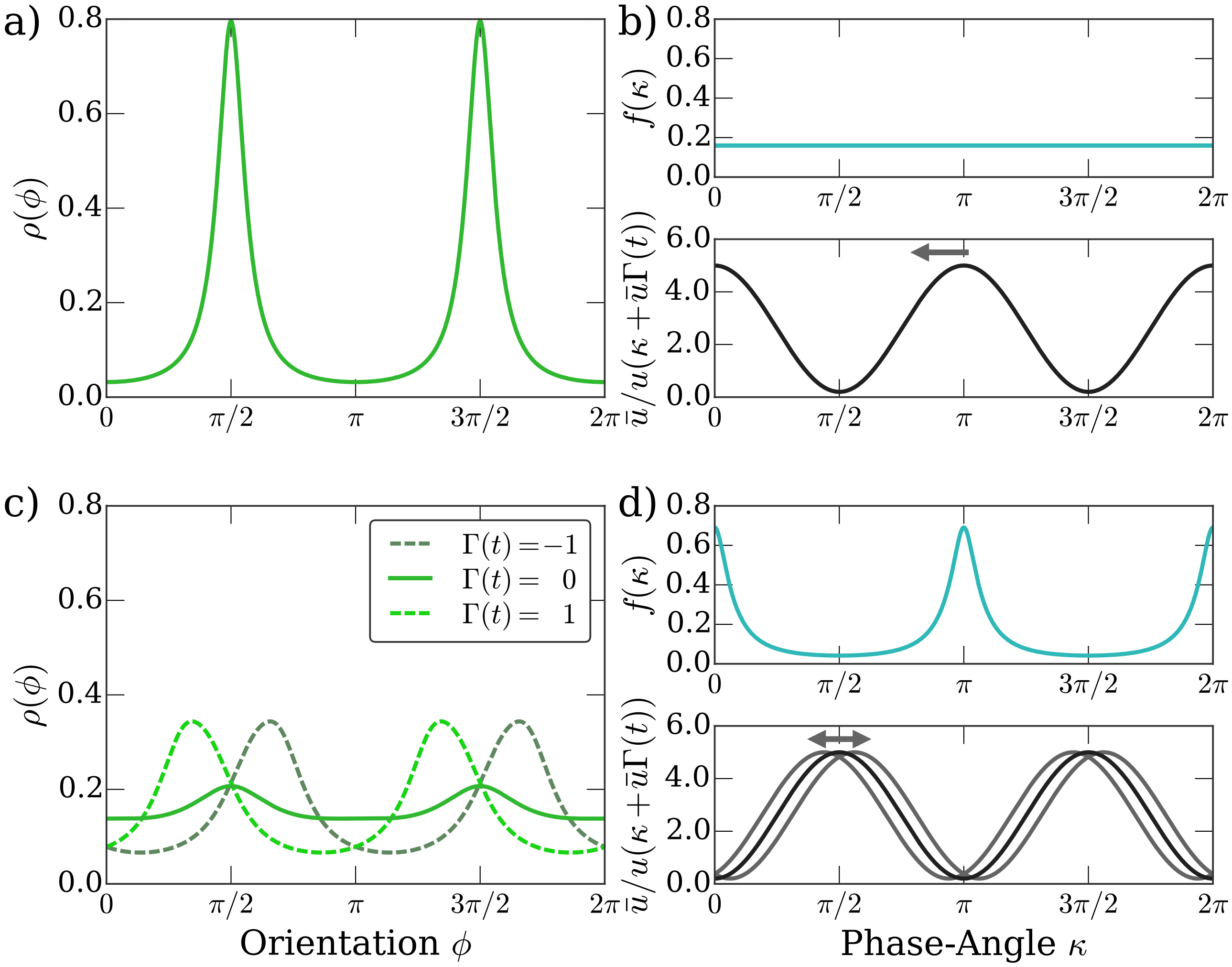

FIG. 1. (a) $\rho(\phi)$ for particles with aspect ratio $r = 5.0$ under steady shear is sharply peaked and constant in time. (b) The corresponding phase-angle distribution $f(\kappa)$ (upper panel) is constant in κ and time. The sharp-peaks of $\rho(\phi)$ correspond to the sharp peaks in the prefactor $\bar{\omega}/\omega$ that multiply $f(\kappa)$. The prefactor translates as the strain increases, leaving $\rho(\phi)$ unchanged in time as $f(\kappa) = 1/2\pi$ is constant in κ. (c) $\rho(\phi)$ under oscillatory shear $\Gamma(t) = 1.0\sin(t)$ changes in a complicated manner with time, stretching and rotating with the flow. In contrast, the phase-angle picture in (d) is much simpler. $f(\kappa)$ does not change with time (top), and has a peak near $\kappa = 0$ and $\kappa = \pi$. The time-varying $\rho(\phi)$ corresponds to the motion of the prefactor $\bar{\omega}/\omega$ in time (bottom, motion indicated by arrows), as its peaks and troughs align with various features in $f(\kappa)$.

orientation alignment determines the optical activity of a suspension [20]. For many processes, such as extruding fiber-reinforced composites, the alignment is desired at a specific moment in time, e.g., when the composite is cured or when the dichroism is measured, rather than over the entirety of the cycle. Motivated by this, we look for a waveform that maximizes the particle alignment at one point in time. For processing applications, this alignment could be locked in by rapidly curing the suspension into a solid matrix. Alternatively, a strong alignment at one point in the cycle could be used to calibrate orientation measurements such as flow dichroism with a strong signal.

As a simple measure of alignment, we look for the waveform that maximizes the largest value of $\rho(\phi)$ at one instant in time. The high symmetry of the Jeffery orbit ensures that maximizing $\rho(\phi)$ produces a highly aligned distribution and prevents pathological distributions, such as a $\rho(\phi)$ with many large peaks along different directions. Moreover, empirically the optimal waveforms that maximize $\rho(\phi)$ are identical to the waveforms that maximize many of the more realistic order parameters, including the standard rank-two liquid crystal order parameters $\boldsymbol{Q}$ and S_2 for dichroism and conductivity, where $\boldsymbol{Q}$ is the traceless, symmetric, second-order orientation tensor ($\boldsymbol{Q} = 2\langle \boldsymbol{pp}\rangle - \boldsymbol{\delta}$ in two dimensions) and S_2 is its maximal eigenvalue.

We maximize the largest value of ρ by first parameterizing the waveforms by 60 Fourier coefficients and optimizing over those coefficients. Without loss of generality, we optimize the value of ρ at the start of an oscillatory cycle. Likewise, there is a gauge freedom in selecting an overall offset for $\Gamma(t)$, corresponding to any transient shear done on the suspension infinitely far in the past; we choose $\Gamma(0) = 0$ throughout the paper. Surprisingly, the optimal waveforms for maximal alignment and for the other properties considered later in this paper have extremely simple forms. As a result, both for maximizing ρ and for the rheology waveforms considered later, we first optimize using the 60 Fourier coefficients to find the simple optimal waveform, then reoptimize using the simpler waveform. The simple optimal waveform always produces more extremal values of the desired property than the naive Fourier parameterization.

Figure 2(a) shows the waveform that maximizes the alignment in a dilute suspension of rods with aspect ratio $r = 5.0$, after the initial transients have decayed. The waveform involves not shearing for almost all of the cycle, then straining by $\Gamma = \pi(r + 1/r)/2 \approx 8.17$, precisely one-quarter of a Jeffery orbit. For the optimal waveform, the duration of this spike goes to zero; panel (a) shows the spike at finite width for ease of viewing. Even for the moderate aspect ratio $r = 5.0$, this waveform produces an exceptionally strong alignment, as shown in panel (b). The peak of the orientation distribution ρ for the optimal waveform (green curve) is 5× greater than that for steady shear (black dotted curve), even though the suspension is not being sheared for most of the optimal cycle!

Why is this alignment so strong compared to steady shear? While the answer is not immediately obvious when examining the behavior of Eq. (4) in terms of $\rho(\phi)$, it is readily apparent in terms of $f(\kappa)$. There are two terms that determine the orientation distribution $\rho(\phi)$ in Eq. (5): A prefactor $\bar{\omega}/\omega$ that does not depend on the waveform but changes during a cycle, and the phase-angle distribution $f(\kappa)$ that depends on the waveform but does not change during a cycle. The prefactor $\bar{\omega}/\omega$ varies strongly with κ, having a strong $\propto r$ peak at $\kappa + \bar{\omega}\Gamma(t) = \pi/2$. Under steady shear, the particle phase angle is completely randomized—$f(\kappa) = 1/2\pi$—and the alignment of ρ arises solely from the peaks in $\bar{\omega}/\omega$. Thus, from the standpoint of Eq. (5), steady shear is a terrible way to align the distribution! Almost any other waveform will produce variations in $f(\kappa)$, and shifting the peak in $\bar{\omega}/\omega$ over a peak in $f(\kappa)$ will produce a more aligned distribution. To maximize the alignment, we should look for a waveform that creates the maximal peak in $f(\kappa)$, and then attempt to add a negligible motion on top of that waveform to align the peak in $f(\kappa)$ with that in $\bar{\omega}/\omega$.

One waveform with a strongly peaked $f(\kappa)$ is low-amplitude sinusoidal shear. As the amplitude of the sinusoidal shear approaches zero, the orientation distribution $\rho(\phi)$ becomes isotropic. The isotropic $\rho(\phi)$ implies that $f(\kappa)$ is strongly peaked, with a magnitude $\sim r$ as $r \to \infty$, since $\rho(\phi) = \bar{\omega}/\omega \times f(\kappa)$ and since $\bar{\omega}/\omega$ varies strongly with κ,

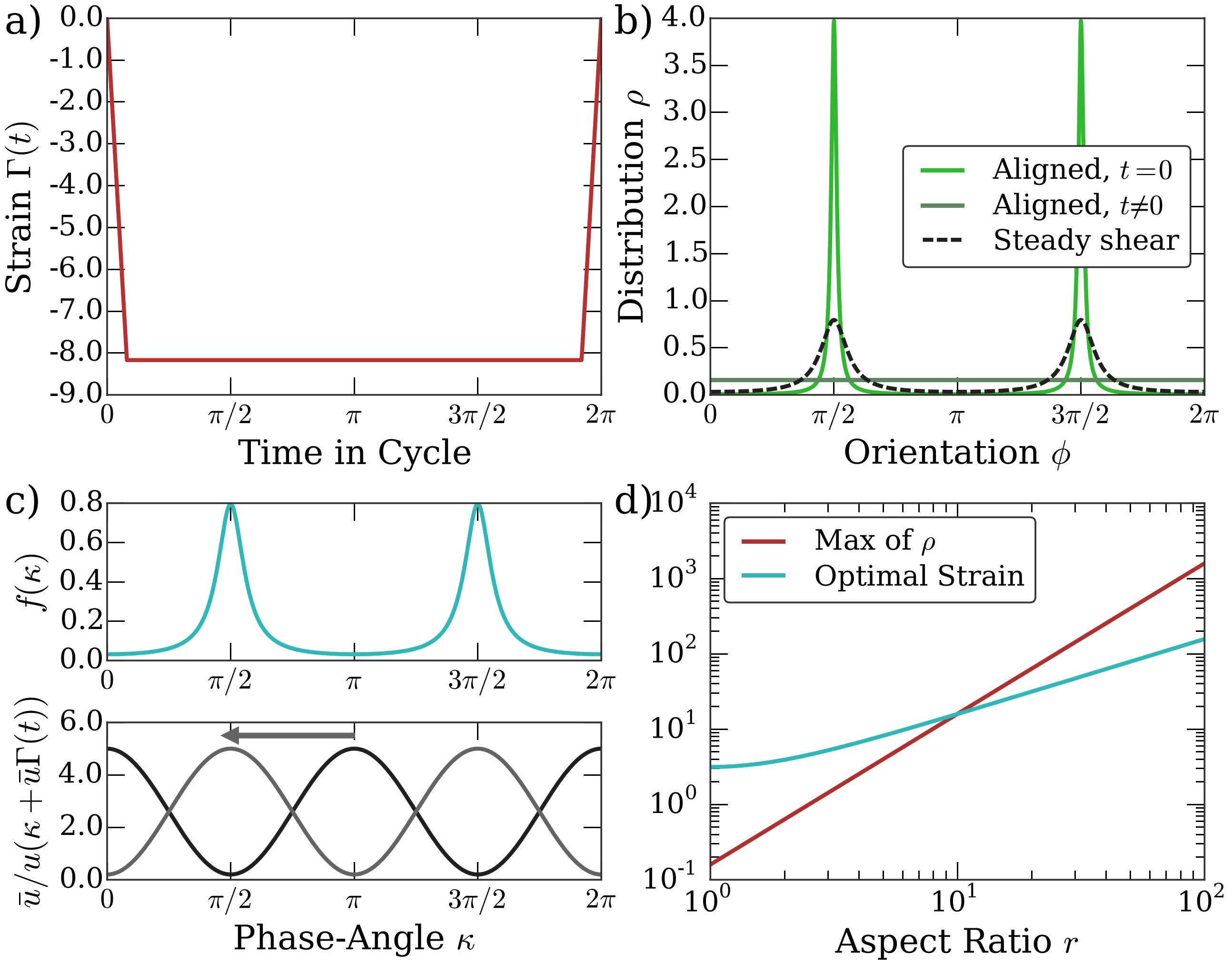

FIG. 2. (a) The spike waveform that maximizes alignment for $r = 5.0$. The optimal waveform has a spike of zero width; panel a shows one of width $\pi/5$ for clarity. (b) The maximally aligned $\rho(\phi)$ (light green) is much more strongly peaked than the steady-shear $\rho(\phi)$ (dotted black), even at moderate $r = 5.0$. When the alignment is not required, the waveform returns the distribution to isotropy (dark green). (c) $f(\kappa)$ (top) for the spike waveform. The prefactor $\bar{\omega}/\omega$ starts antialigned with $f(\kappa)$ (black curve), and translates to align its peak with that of $f(\kappa)$ (gray curve), as indicated by the arrow. (d) The maximal value of $\rho(\phi)$ (red) and the optimal strain (cyan), as a function of r (multimedia view in the supplementary material).

cf. Eq. (5). From the naive viewpoint of $\rho(\phi)$, zero-amplitude sinusoidal shear is a terrible way to align particles, as $\rho(\phi) = 1/2\pi$ is completely isotropic. But from the viewpoint of the phase-angle distribution, this waveform is a great way to align the distribution, since $f(\kappa)$ is sharply peaked. The only slight problem is that, at zero strain, the prefactor $\bar{\omega}/\omega$ exactly cancels any peaks in $f(\kappa)$. However, this problem is easily rectified by straining by an amount exactly 1/4 of a Jeffery orbit $\Gamma = \pi(r + 1/r)/2$, aligning the peak of $\bar{\omega}/\omega$ with that of $f(\kappa)$. Moreover, since $\mathfrak{D}(\kappa)$ and $f(\kappa)$ are determined by time-averages of the waveform [cf. Eq. (7)], a rapid shift in strain will not affect the phase-angle distribution $f(\kappa)$.

This approach is precisely what the optimal waveform in Fig. 2 takes. Not shearing for most of the cycle creates the sharply peaked $f(\kappa)$ shown in panel (c), which is the same as under zero-amplitude shear except for a shift resulting from our choice of $\Gamma(0)$. This creates an orientation distribution which is completely isotropic throughout most of the cycle. Then, exactly at the start of the cycle, the waveform shifts the peak of $\bar{\omega}/\omega$ to align with the peak of $f(\kappa)$, giving a strongly aligned orientation distribution

$$\rho(\phi) = \frac{1}{2\pi} \frac{1}{r^2 \cos^2 \phi + r^{-2} \sin^2 \phi}. \tag{9}$$

The peak of height $r/2\pi$ in $f(\kappa)$ and the peak of height r in $\bar{\omega}/\omega$ cooperate to produce the $r^2/2\pi$ peak in $\rho(\phi)$. Aligning the peaks in $f(\kappa)$ and $\bar{\omega}/\omega$ requires a strain of 1/4 of a Jeffery orbit, or $\pi(r + 1/r)/2$. As shown in Fig. 2(d), both the optimal strain and the maximal alignment follow the predicted strain scalings.

This mechanism has a simple explanation in terms of $\rho(\phi)$ and the velocity field of the Jeffery orbit. As the suspension is not sheared for most of the cycle, diffusion relaxes the orientation distribution to isotropy, except for during the waveform's spike, cf. Fig. 2 (multimedia view in the supplementary material) [21]. This isotropic distribution corresponds to orienting a sizeable fraction of the particles near the gradient direction, where the Jeffery orbit rotates rapidly. The spike then rotates these particles by one-fourth of a Jeffery orbit, aligning them near the flow direction. The Jeffery orbit rotational velocity is suppressed by $\sim 1/r^2$ compared to the velocity near the gradient direction, resulting in the $\sim r^2$ bunching of particles visible in Fig. 2. This strong alignment also occurs at startup of steady shear, when the accumulated strain is exactly one-fourth of a Jeffery orbit. However, as the steady shear continues the orientation distribution relaxes to its less-aligned long-time value. By returning the orientation distribution back to isotropy, the spike waveform is able to repeat this strong alignment indefinitely many times.

While the above argument shows that a $\sim r^2$ particle alignment is possible, it does not prove that the spike waveform in Fig. 2(a) is the optimal one nor divulge how robust it is to deviations from perfection. We can further understand the optimal waveform by delving deeper into the functional form of $\mathfrak{D}(\kappa)$. Expanding out the sines and cosines in Eq. (7) gives a simplified form for $\mathfrak{D}(\kappa)$

$$\begin{aligned}\mathfrak{D}(\kappa)/D &= \frac{3}{8}(r - 1/r)^2 + 1 - \frac{1}{2}(r^2 - 1/r^2) A_2 \cos(2\kappa + \delta_2) \\ &\quad + \frac{1}{8}(r - 1/r)^2 A_4 \cos(4\kappa + \delta_4), \quad \text{where} \\ A_n e^{i\delta_n} &= \frac{1}{T_{cyc}} \int_0^{T_{cyc}} e^{in\Gamma(t)/(r+1/r)}\, dt. \end{aligned} \tag{10}$$

Only four real coefficients (A_2, δ_2, A_4, δ_4) describe the entirety of the infinite-dimensional space of possible waveforms, through $\cos(2\kappa)$ and $\cos(4\kappa)$ oscillations in $\mathfrak{D}(\kappa)$. In general, either $A_2 e^{i\delta_2}$ or $A_4 e^{i\delta_4}$ can take any values in the complex unit disk, although they cannot be varied completely independently of each other. For some simple oscillatory waveforms, these coefficients can be calculated exactly—for example, for sinusoidal shear $\Gamma(t) = \Gamma_0 \sin(2\pi f t)$ the coefficients are $A_2 = J_0(2\Gamma_0/(r + 1/r))$, $\delta_2 = 0$ and $A_4 = J_0(4\Gamma_0/(r + 1/r))$, $\delta_4 = 0$, where J_0 is the zeroth-order Bessel function—but for a generic waveform these coefficients are not expressible analytically. Nevertheless, Eq. (10) still divulges much information about a generic waveform. Since A_n, δ_n are determined by time-averages, waveforms that only deviate from one another for a short time will have similar phase-angle distributions. Since $f(\kappa) \propto 1/\sqrt{\mathfrak{D}(\kappa)}$, waveforms for which A_2 and A_4 are small will create phase-angle distributions with relatively little variation in κ. As A_2 and A_4 increase, the variations in $\mathfrak{D}(\kappa)$ and $f(\kappa)$ increase as well. Tuning A_2 and A_4 toward their maximal values of 1 creates small minima in $\mathfrak{D}(\kappa)$, corresponding to a highly aligned $f(\kappa)$.

The coefficients A_2 and A_4 describe the effect of a finite-width spike on the alignment. Since $\rho = \bar{\omega}/\omega \times f(\kappa)$, and since $f(\kappa) \propto 1/\sqrt{\mathfrak{D}(\kappa)}$, a highly aligned distribution can occur when $\mathfrak{D}(\kappa)$ has a small minimum. For a perfect waveform with an infinitesimal spike width, $A_2 = A_4 = 1$. The minimum of $\mathfrak{D}(\kappa)$ occurs when $\cos(2\kappa + \delta_2) = \cos(4\kappa + \delta_4) = 1$, which occurs at $\kappa = \pi/2$ for the choice of $\Gamma(0) = 0$ shown in Fig. 2. This value of κ cancels both the $O(r^2)$ and the $O(1)$ terms in $\mathfrak{D}(\kappa)$, creating a minimum value of $\mathfrak{D}(\kappa) \sim 1/r^2$ when r is large. Since $f(\kappa) \propto 1/\sqrt{\mathfrak{D}(\kappa)}$, this minimum corresponds to a $\propto r$ peak in $f(\kappa)$, which creates the $\propto r^2$ alignment in ρ as the spike aligns the peak in $\bar{\omega}/\omega$ with that in $f(\kappa)$.

When the spike has a small but finite width w, both A_2 and A_4 decrease by an amount proportional to w. As visible from Eq. (10), this finite width will change $\mathfrak{D}(\kappa)$ by an amount $\propto wp^2$ when r is large. To change the peak in $f(\kappa)$ by a small fractional amount, the $\propto 1/r^2$ minimum in $\mathfrak{D}(\kappa)$ must also change by a small fractional amount. Thus, the wp^2 change in $\mathfrak{D}(\kappa)$ must be comparable to the $1/r^2$ minimum in the ideal $\mathfrak{D}(\kappa)$, or $w \lesssim 1/r^4$ for the width of the spike to have little effect.

The alignment is extraordinarily sensitive to the spike width due to diffusion. The optimal waveform creates a $\sim r^2$ alignment, and therefore ρ changes rapidly on an orientation scale $\ell \sim 1/r^2$. Since the diffusivity enters through $D\nabla^2\rho$, the large gradients effectively enhance the diffusion by an amount $\sim 1/\ell^2 \sim r^4$. The spike duration w ceases to be short enough for diffusion to appreciably affect the distribution when $wp^4 \approx 1$, requiring an extremely brief spike duration before diffusion begins to smooth out the distribution.

Figure 3 shows the effect of a finite spike duration on the distributions. Panel (a) shows $f(\kappa)$ for a particle of aspect ratio $r = 5.0$, for spike strains $\Gamma = \pi(r + 1/r)/2$ and spike widths varying from 0 (cyan) to 2π (i.e., triangle-wave shear, in black). Since a spike width of $\sim 1/r^4$ produces a significant decrease in the peak of $f(\kappa)$, even at moderate $r = 5.0$ a spike that occupies 1% of the duration of the cycle significantly decreases the peak value of $f(\kappa)$. This peak value decreases rapidly with increasing spike width [panels (a) and (b)], which correspondingly decreases the maximal value of $\rho(\phi)$ [panel (c)]. Even with these finite widths, however, the spike waveform always aligns $\rho(\phi)$ more than steady shear does. Panel (d) shows the scaling of the alignment with aspect ratio. While a spike of infinitesimal width creates a $\sim r^2$ orientational alignment, any fixed-width spike reduces the scaling to $\sim r$, as shown by the curves for a spike width of $\pi/5$ [the waveform in Fig. 2(a)] and of width $\pi/500$, although either width always results in significantly more enhancement than steady shear. In contrast, decreasing the spike width with aspect ratio as $w = 1/r^4$ aligns the distribution to $\approx$91% of its ideal value.

How achievable are these strong alignments in practice? There are two necessary requirements for a strong alignment to be achieved: The rotary Péclet number $\mathrm{Pe} = 1/DT_{cyc}$ must be large, and the spike duration must be small ($w < 1/r^4$). One fundamental source of a finite-spike duration is the time for the shear flow to develop due to fluid inertia. For simple shear created by two plates separated by a distance h, this flow development time is $t \approx h^2/\nu$, where ν is the kinematic viscosity of the liquid. The constraint that the development time be small compared to $1/r^4$ implies that the cycle period must be at least $T_{cyc} > r^4 h^2/\nu$. Increasing the viscosity of the suspending fluid will decrease the flow development time proportionately, making the rapid spike easier to achieve. In addition to having a rapid spike duration, the Péclet number must also be large. Requiring $\mathrm{Pe} > 100$ bounds the cycle duration from above as $T_{cyc} < 1/100D$. For a fixed cycle duration and particle size, increasing the suspending fluid's viscosity will proportionately decrease the rotational diffusivity, making both the high-Péclet requirement and the rapid spike duration

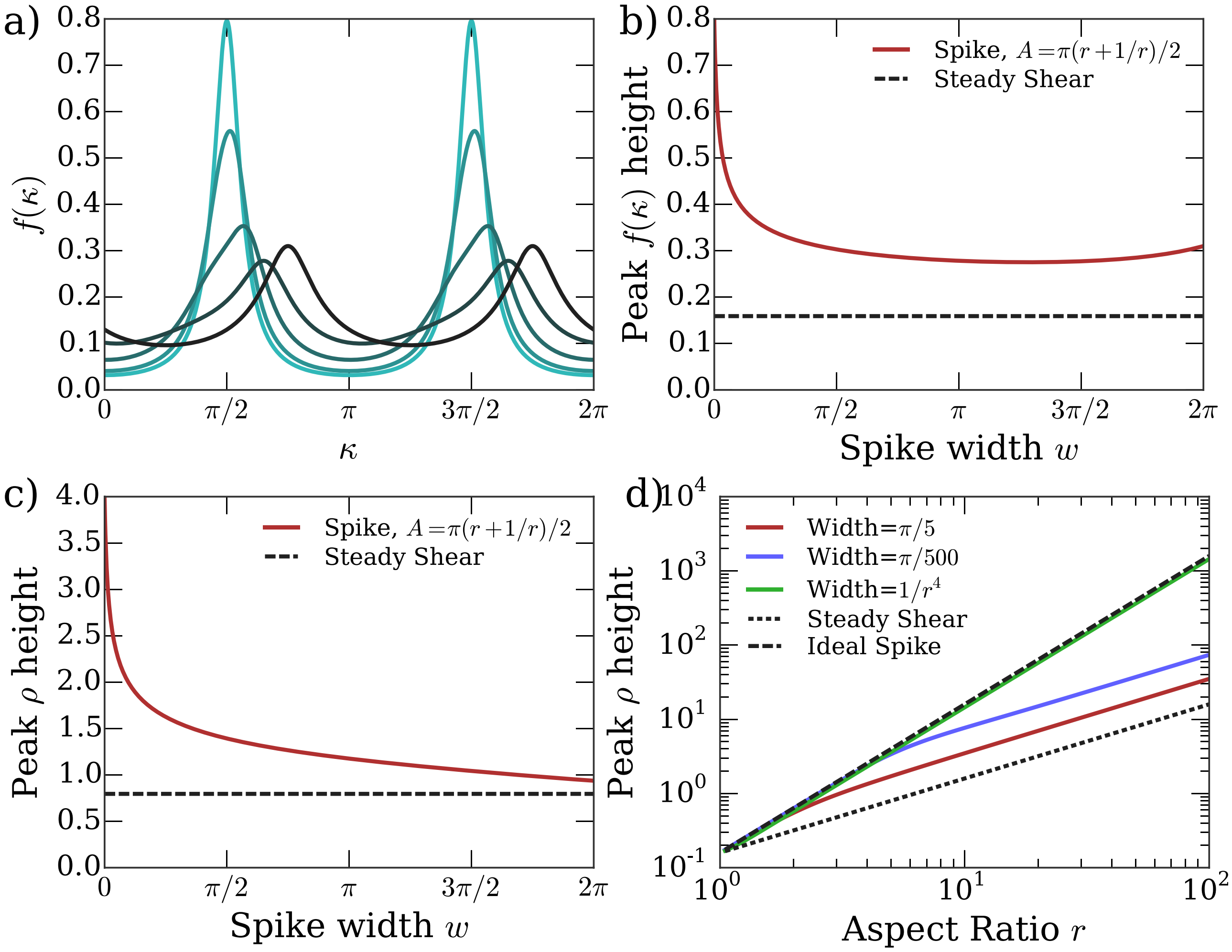

FIG. 3. Effect of finite spike width on distribution alignment. (a) $f(\kappa)$ for a spike waveform, with spike widths of 0% (cyan), 1%, 10%, 50%, and 100% (black) of the triangle-wave limit of 2π, at fixed amplitude $\Gamma = \pi(r + 1/r)/2$ and for a suspension with $r = 5$. (b) The peak height of $f(\kappa)$ as a function of the spike width; in general the peak height decreases as the spike width increases, but it always remains considerably greater than the constant $f(\kappa)$ for steady shear (dashed line). (c) The maximum of $\rho(\phi)$ for a spike waveform as a function of the spike width, with the spike centered at $t = 0$. (d) The scaling of the maximal $\rho(\phi)$ as a function of aspect ratio for steady shear (dotted black line), a spike of fixed width $\pi/5$ like that in Fig. 2 (red), a spike of fixed width $\pi/500$ (blue), a spike of width $1/r^4$, and for an ideal spike of infinitesimal width (dashed black line).

easier to achieve. These requirements constrain the cycle duration as

$$\left(\frac{r}{5}\right)^{4}\left(\frac{h}{1\,\mathrm{cm}}\right)^{2}\frac{0.0008\,\mathrm{m}^2/\mathrm{s}}{\nu}\times 79\,\mathrm{s} < T_{cyc} < 1400\,\mathrm{s} \times\left(\frac{\eta}{1\,\mathrm{Pa}\cdot\mathrm{s}}\right)\left(\frac{a}{5\,\mu\mathrm{m}}\right)^{3}; \tag{11}$$

the numbers are for a $r = 5.0$ particle in pure glycerol with long axis of $a = 5\,\mu$ m, between two plates 1 cm apart, and the rotational diffusivity is calculated using the asymptotic mobility relationships from [22] for a $r = 5$ spheroid; the mobility increases logarithmically slowly as r increases from 5. Thus, for a moderately sized particle in a viscous solvent, an ideal spike waveform should be easy to achieve. If a solvent with the viscosity of water is used with the same particle, the plate separation needs to be decreased to 40 μm for this inequality to be achievable, with a cycle duration of about 1 s. However, as Fig. 3(d) shows, while increasing the spike duration decreases the alignment, the spike waveform always produces a stronger alignment than continuous shear. Thus, as long as the flow development time is short compared to a cycle the spike waveform will strongly align the particles, although not as well as the ideal spike.

IV. MAXIMIZING AND MINIMIZING VISCOSITY

Colloidal rods are a classic model system for exploring non-Newtonian rheological behaviors, with the first investigations dating back almost 100 years [1,23]. Even dilute suspensions in simple shear flows can exhibit interesting non-Newtonian behavior such as shear-thinning, stress overshoots, and normal stresses [24–27], arising from a combination of viscoelastic, flow-memory, and relaxation effects [8, 28–31]. This non-Newtonian behavior arises because the particle orientations both couple to the flow and affect the suspension stress. As rodlike particle suspensions produce a wide array of rheological behaviors even for simple flows, we expect that we can strongly control their rheology under arbitrary-waveform oscillatory shear flows.

The stress at one instant in time in a suspension of rodlike particles is determined by the current strain rate and moments of the particle orientations

$$\begin{aligned}\boldsymbol{\sigma} = 2\eta\mathbf{E} + 2\eta c\Big\{&2A_H(\mathbf{E}:\langle\boldsymbol{pppp}\rangle - \mathbf{I}\,\mathbf{E}:\langle\boldsymbol{pp}\rangle)\\ &+2B_H\left(\mathbf{E}\cdot\langle\boldsymbol{pp}\rangle + \langle\boldsymbol{pp}\rangle\cdot E - \frac{2}{3}\mathbf{I}\,\mathbf{E}:\langle\boldsymbol{pp}\rangle\right)\\ &+C_H\mathbf{E} + F_H D\left(\langle\boldsymbol{pp}\rangle - \frac{1}{3}\mathbf{I}\right)\Big\},\end{aligned} \tag{12}$$

where $\mathbf{E}$ is the instantaneous rate-of-strain tensor of the fluid, $\mathbf{I}$ is the identity, η is the suspending fluid viscosity, c is the volume fraction of rods, and A_H, B_H, C_H, and F_H are shape-dependent hydrodynamic coefficients [4,7,8,22,32]. At high Pe, the potentially elastic Brownian stress in the last term is negligible compared to the other terms, and the suspension stores no elastic energy.

For particles confined to the flow-gradient plane at high Pe, these equations simplify considerably. The increase in the effective shear viscosity due to the particles, per unit concentration and normalized by the fluid viscosity, is

$$(\boldsymbol{\sigma}/2\eta - \mathbf{E})_{xy}/c = A_H\langle 1 - \cos 4\phi\rangle/8 + B_H + C_H. \tag{13}$$

As a result, for particles orientations confined to the flow-gradient plane, controlling the shear stress in a suspension only involves controlling the $\langle\cos 4\phi\rangle$ moment of the distribution. As Eqs. (12) and (13) show, at high Pe the suspension response is always proportional to the instantaneous strain rate and never has an elastic component. However, since the particle orientations change with time, the proportionality constant in Eq. (13) between the stress and the strain rate changes with time, producing a purely viscous but non-Newtonian response. We call this proportionality constant the instantaneous viscosity $\eta(t)$, as it can change during an oscillatory shear cycle. After the initial transients have decayed, this non-Newtonian $\eta(t)$ arises from the suspension's memory of the average waveform through $\mathfrak{D}(\kappa)$ [9].

The instantaneous viscosity provides information about the particle properties through the hydrodynamic coefficients A_H, B_H, C_H, which depend on the particle shape. In a typical rheological measurement at high Pe all three coefficients are measured simultaneously. For idealized particle orientations confined to the flow-gradient plane, it is impossible to separately measure the coefficients B_H and C_H from the shear stress. However, the coefficient A_H can be measured from two separate waveforms that produce separate particle distributions, cf. Eq. (13). Ideally, these two waveforms should produce an $\eta(t)$ that is maximally different from one another. Motivated by this, we look for the waveforms that maximize and that minimize $\eta(t)$, after the decay of initial transients. For simple waveforms such as steady shear or sinusoidal shear, the suspension viscosity $\eta(t)$ is simply related to the suspension stress. For more complex waveforms, these two can differ dramatically, as the shear rate can be small or even zero when the viscosity is large. As a result, a waveform that extremizes the viscosity will not in general extremize the measured stress. However, an additional high-frequency, small-amplitude "probe" flow will measure the viscosity that is created by the "pump" waveform. The probe flow will not change the distributions, since $f(\kappa)$ and $\mathfrak{D}(\kappa)$ only depend on the average strain and not on the strain rate [cf. Eq. (7)]. Since the time-average value that the probe will measure is the time-average of the viscosity, we maximize and minimize the long-time ($Dt \gg 1$) average of $\eta(t)$, denoted by $\langle\eta(t)\rangle_t$. In addition, the extremal $\langle\eta(t)\rangle_t$ waveforms are simple to analyze, as the viscosity depends only on the strain waveform and not directly on the strain rate.

As for the case with maximizing the distributions, extremizing the viscosity is simpler in terms of $f(\kappa)$. Since $f(\kappa)\,d\kappa = \rho(\phi)\,d\phi$ by construction, the average in Eq. (13) can also be taken in phase-angle space instead of orientation space: $\langle\cos(4\phi)\rangle = \int\cos(4\phi)\rho(\phi)\,d\phi = \int\cos(4\phi(\kappa+\varpi\Gamma))\,f(\kappa)\,d\kappa$. From this standpoint, the waveform $\Gamma(t)$ determines

$f(\kappa)$, which does not change in time. Instead, during a cycle, the strain shifts the position of $\cos(4\phi)$ in κ space, and the nonlinear transformation between ϕ and κ warps its shape. Maximizing or minimizing the viscosity then corresponds to selecting a waveform that maximizes or minimizes the overlap between $\cos(4\phi)$ and the $f(\kappa)$ that the waveform creates.

Figure 4(a) displays the waveform that maximizes $\langle\eta(t)\rangle_t$ for a suspension of particles with aspect ratio $r = 5.0$ (dashed brown line). Similar to the waveform that maximizes $\rho(\phi)$, during most of the cycle the suspension is not sheared. In contrast to the waveform in Fig. 2, however, the waveform that maximizes the time-averaged viscosity spends an equal amount of time at two separate strains: At a strain $\Gamma = 0$ and at $\Gamma \approx 1.26$. Since the difference between these strains is relatively small, this waveform creates a well-peaked $f(\kappa)$ [a dashed curve, upper portion of panel (b)] with the peak slightly offset from $\kappa = 0$. At $\Gamma = 0$, the peak in $f(\kappa)$ aligns with the peak at $\phi = -\pi/4$ in the stress term $(1 - \cos 4\phi)/8$ from Eq. (13). Increasing the strain to $\Gamma = 1.26$ aligns the second peak at $\phi = +\pi/4$ with the peak of $f(\kappa)$. Aligning the peak in $f(\kappa)$ with a peak in the stress term creates a large viscosity, while alternating the alignment between the two peaks keeps the suspension sheared and prevents it from relaxing to isotropy. As a result, the viscosity is large and constant during the cycle, except for two small dips as the strain changes from $\Gamma = 0$ to $\Gamma = 1.26$, cf. panel (c).

This explanation in phase-angle space has a simple analog in orientation space. The viscosity is largest when the orientations are aligned along the flow's principle strain axes at $\phi = \pm\pi/4$, cf. Eq. (13). The waveform first aligns the particles with the axis at $\phi = -\pi/4$ before rotating to the other axis at $\phi = \pi/4$ by rapidly sweeping the orientations through the gradient axis at $\phi = 0$, as shown in Fig. 4(d). Aligning the particle orientations along these principle axes keeps the viscosity large throughout the cycle. Since the Jeffery orbit rotates particles rapidly in the angles between $\phi = -\pi/4$ and $\phi = \pi/4$, alternating the alignment between the two axes only requires the small, $O(1)$ strain shown in Fig. 4. The boxcar waveform's oscillation between two strain values

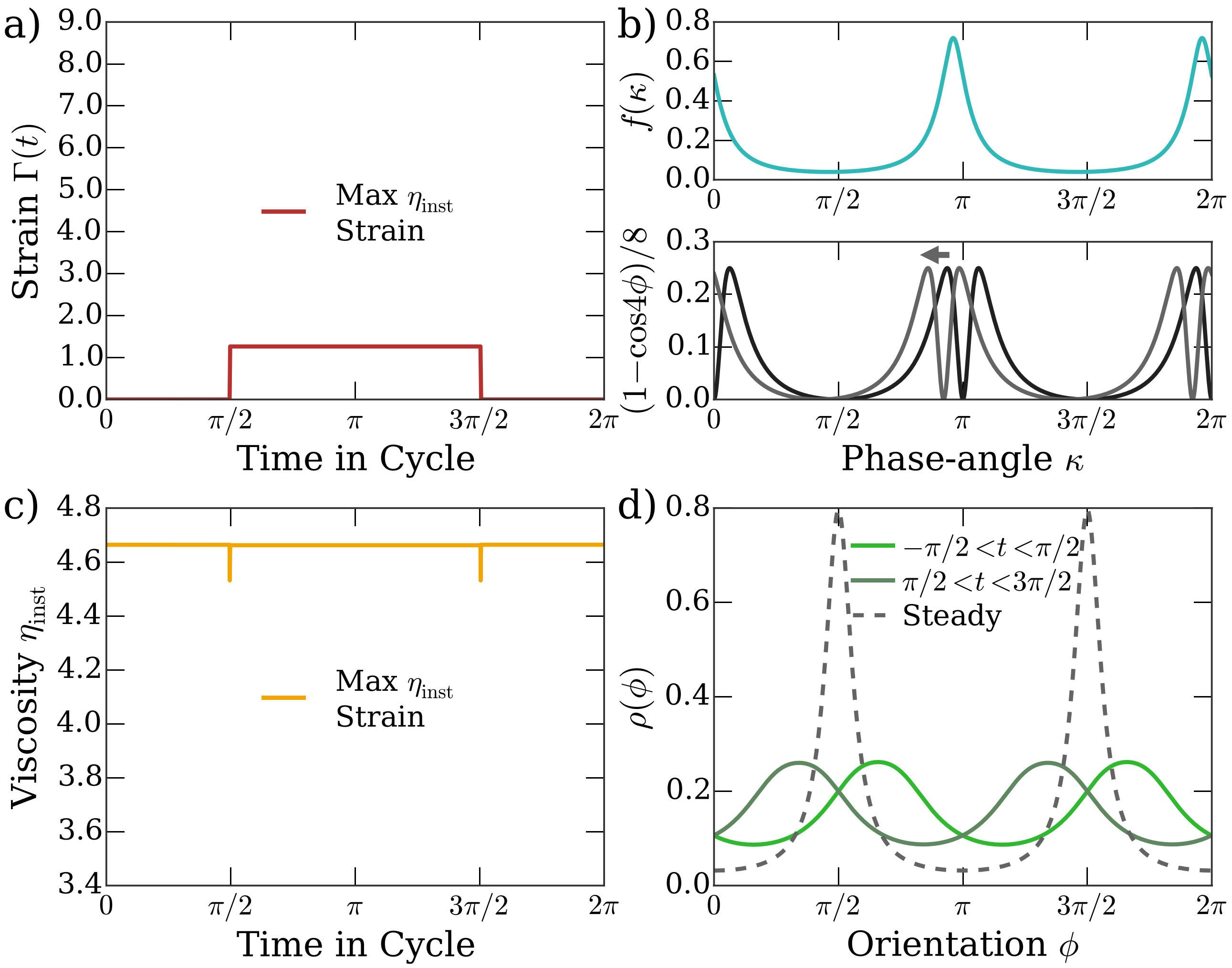

FIG. 4. (a) The waveform that maximizes $\langle\eta(t)\rangle_t$, for a suspension with $r = 5.0$. The optimal waveform has a ramp-width of zero, as shown in the figure. (b) Top panel: The corresponding phase-angle distribution. Bottom panel: The stress term at the start of the cycle (black) and at the middle of the cycle (gray). (c) The viscosity as a function of time in the cycle. (d) The orientation distribution $\rho(\phi)$, for $-\pi/2 < t < \pi/2$ (light green) and for $\pi/2 < t < 3\pi/2$ (dark green), with the continuous shear distribution (a dotted line) for comparison. Since the waveform is symmetric under time reversal, the two distributions are symmetric under a reflection about the gradient axis. The large viscosity results from orienting the particles along the principle strain axes at $\phi = (2n+1)\pi/4$ (multimedia view in the supplementary material).

prevents the distribution from ever relaxing to isotropy [Fig. 4(d) (multimedia view in the supplementary material)].

Once the Fourier search indicates that a boxcar waveform is optimal, a simple derivation leads to an analytical expression for the distributions $f(\kappa)$ and $\rho(\phi)$. For a boxcar that alternates between a strain of 0 and Γ_0, Eq. (7) shows

$$\mathfrak{D}(\kappa) = \left\{ \frac{1}{2}\left[\frac{\bar{\omega}}{\omega(\kappa)}\right]^2 + \frac{1}{2}\left[\frac{\bar{\omega}}{\omega(\kappa+\bar{\omega}\Gamma_0)}\right]^2 \right\}.$$

Substituting in Eqs. (5) and (8) gives $\rho(\phi)$ during the zero-strain portion of the waveform as

$$\rho(\phi) = \frac{f(\kappa(\phi))}{\omega/\bar{\omega}} \propto \left[1 + \frac{\omega(\kappa(\phi))^2}{\omega(\kappa(\phi)+\bar{\omega}\Gamma_0)^2}\right]^{-1/2},$$

with a similar expression for ρ at strain Γ_0. When the suspension is not being sheared, diffusion begins to relax $\rho(\phi)$ back to isotropy. In κ-space, diffusional relaxation corresponds to either increasing or decreasing $f(\kappa)$, depending on whether the corresponding value of κ maps to a region where $\rho(\phi)$ is depleted or enhanced. The stationary $f(\kappa)$ is the distribution such that any decreases in $f(\kappa)$ at $\Gamma(t) = 0$ are exactly canceled by increases in $f(\kappa)$ when $\Gamma(t) = \Gamma_0$. In general, this stationary $f(\kappa)$ produces an orientation distribution $\rho(\phi)$ that is different in the two regions of the waveform and that is not isotropic, even though the strain rate is almost always zero.

The waveform that minimizes the time-averaged shear viscosity is similar to the one that maximizes it, as shown by the solid red line in Fig. 5(a). The waveform is also a boxcar, alternating between a strain of $\Gamma = 0$ and $\Gamma \approx 8.17$. However, while the waveform is similar to the one that maximizes $\langle \eta(t) \rangle_t$, the two phase-angle distributions $f(\kappa)$ differ significantly. As the strain $\Gamma = 8.17$ is relatively large, $f(\kappa)$ no longer has a sharp peak, but is almost constant with small, $\cos(4\kappa)$ oscillations, shown by the solid line in panel (b). These oscillations create a minimum in $f(\kappa)$ at $\kappa = \pi$, near the double-peak of the stress term. The waveform then shifts this double-peak from the trough in $f(\kappa)$ at $\kappa = \pi$ to the trough at $\kappa = \pi/2$. Eliminating any peaks in $f(\kappa)$ prevents a

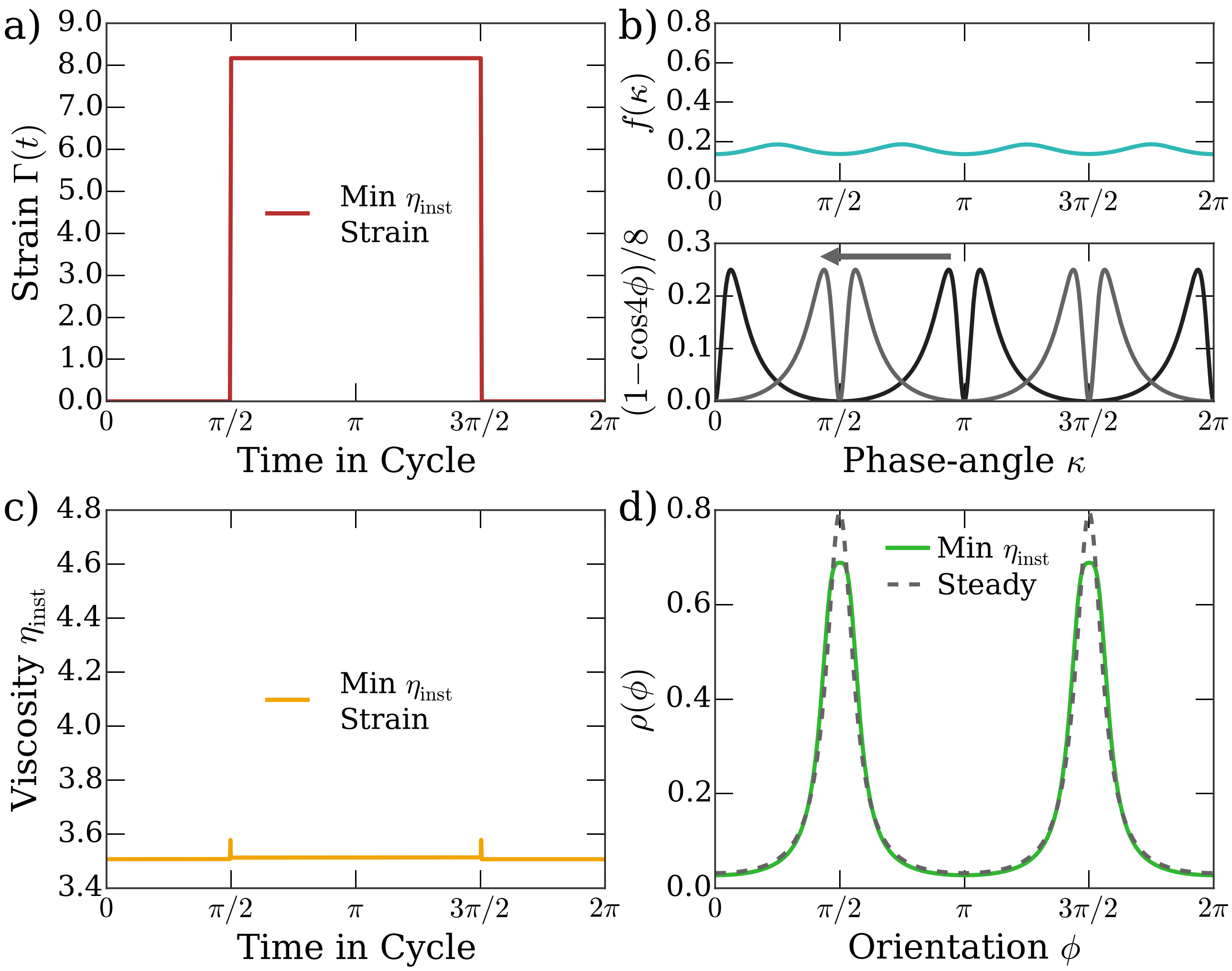

FIG. 5. (a) The waveform that minimizes $\langle \eta(t) \rangle_t$, for a suspension with $r = 5.0$. The optimal waveform has a ramp-width of zero, as shown in the figure. (b) Top panel: The corresponding phase-angle distribution. Bottom panel: The corresponding stress term at the start of the cycle (black) and at the middle of the cycle (gray). (c) The viscosity as a function of time in the cycle. (d) The orientation distribution $\rho(\phi)$ (light green), with the continuous shear distribution (a dotted line) for comparison. The minimal viscosity waveform produces a distribution that is identical in both regions of the boxcar waveform. The small viscosity results from orienting the particles away from the principle strain axes at $\phi = (2n+1)\pi/4$ (multimedia view in the supplementary material).

large overlap with the stress term and keeps the viscosity low, while aligning the small minima due to the $\cos(4\kappa)$ oscillations further depresses the viscosity. Alternating the alignment with the different $\cos(4\kappa)$ minima keeps the distribution from relaxing to isotropy. As a result, the viscosity is small and constant during a cycle, except for two small bumps as $\Gamma(t)$ changes from 0 to 8.17, cf. panel (c).

The low-viscosity waveform also has a simple description in orientation space. The viscosity is minimal when the orientations are aligned either along the flow direction, at $\phi = \pm\pi/2$, or along the gradient direction, at $\phi = 0, \pi$, cf. Eq. (13). Steady shear naturally aligns particles along the flow direction and creates the low steady-shear viscosity [7]. The large-amplitude boxcar waveform closely mimics steady shear and strongly decreases the viscosity by aligning particles along the flow direction, as shown in Fig. 5(d) (multimedia view in the supplementary material). The small, $\cos(4\kappa)$ modulations suppress the wider tails of the orientation distribution, reducing the overlap of the distribution with the principle strain axes and further decreasing the viscosity.

From this picture, we can understand the scaling with aspect ratio of the waveform that maximizes $\langle\eta(t)\rangle_t$ and its average viscosity. The waveform aligns the peak in $f(\kappa)$ with the two closely separated maxima in the stress term $(1-\cos 4\phi)/8$, alternating between the two maxima at $\phi = \pm\pi/4$. The nonlinear transformation of ϕ to κ [Eq. (1)] compresses the distance between these two maxima to a separation of $\sim 2/r$ in κ space, as $r \to \infty$. Since a strain Γ shifts the stress term in κ space by an amount $\bar{\omega}\Gamma$, and since $\bar{\omega}$ also scales as $\sim 1/r$, the strain that maximizes $\langle\eta(t)\rangle_t$ is asymptotically constant. This approach to a constant $\Gamma \approx 1.30$ at large r is visible in Fig. 6(d). Since the maximal-$\langle\eta(t)\rangle_t$ waveform aligns the peak in $f(\kappa)$ with the peaks in the stress term, the expectation $\langle 1-\cos(4\phi)\rangle$ is always $O(1)$, and $\langle\eta(t)\rangle_t - B_H - C_H \sim A_H$ as the aspect ratio grows. The scaling of the maximal viscosity in panel (d) reflects this, following the $\sim r^2/\ln r$ scaling of the hydrodynamic coefficient A_H [4].

Next, we examine the scaling with aspect ratio of the waveform that minimizes $\langle\eta(t)\rangle_t$ and of its average viscosity. The minimal waveform alternates between positioning the double-peaks in the stress term on the minima in $f(\kappa)$, at $\kappa = 0$ and $\kappa = \pi/2$. Effecting this $\pi/2$ shift in κ requires a strain $\Gamma = \pi/2\bar{\omega} = \pi(r+1/r)/2$, as shown by the minimal-$\langle\eta(t)\rangle_t$ strain in panel (d). Moreover, this shift of $\Gamma = \pi(r+1/r)/2$ sets the coefficient $A_2 = 0$ in Eq. (10), leaving $f(\kappa)$ with the $\cos(4\kappa)$ modulation visible in the figure. The minimal-$\langle\eta(t)\rangle_t$ waveform eliminates any large peaks from $f(\kappa)$. Since $1-\cos(4\phi)$ only differs significantly from zero in a region of width $\sim 1/r$, the expectation $\langle 1-\cos(4\phi)\rangle$ is $O(1/r)$, and $\langle\eta(t)\rangle_t - B_H - C_H \sim O(A_H/r)$ as the aspect ratio grows. The scaling of the minimal viscosity in panel (d) reflects the $\sim r/\ln r$ scaling expected.

The waveforms that maximize and minimize the viscosity are robust to a finite ramp width even at large r, in contrast to the spike waveform that maximizes $\rho(\phi)$. Increasing the ramp width of the waveform to w results in an $\sim w$ change in the coefficients A_2, A_4. However, neither A_2 nor A_4 equal 1 for the maximal or minimal strain waveforms. Thus, there are no sensitive minima in $\mathfrak{D}(\kappa)$, unlike the case for the maximal $\rho(\phi)$ waveforms, and $\mathfrak{D}(\kappa)$ changes proportional to an $O(w)$ factor everywhere, instead of $O(wr^4)$ in some locations. As a result, replacing the boxcar waveform by a trapezoidal waveform with a small ramp time of duration w changes the maximal and minimal viscosities change by a small $\sim w$ fraction. The difference between the time-averaged viscosities for an infinitesimal ramp width and for a $\pi/5$ ramp width is indistinguishable on the scale of Fig. 6(d).

V. MAXIMIZING NORMAL STRESSES

The presence of hydrodynamic normal stresses is severely restricted by the linearity and reversibility of Stokes flow. Since reversing time corresponds to changing the sign of the shear rate, the linearity of Stokes flow implies that reversing time will change the sign of the stress tensor. Thus, for an oscillatory flow, all hydrodynamic stresses—including normal stresses—must time-average to zero, as an average value

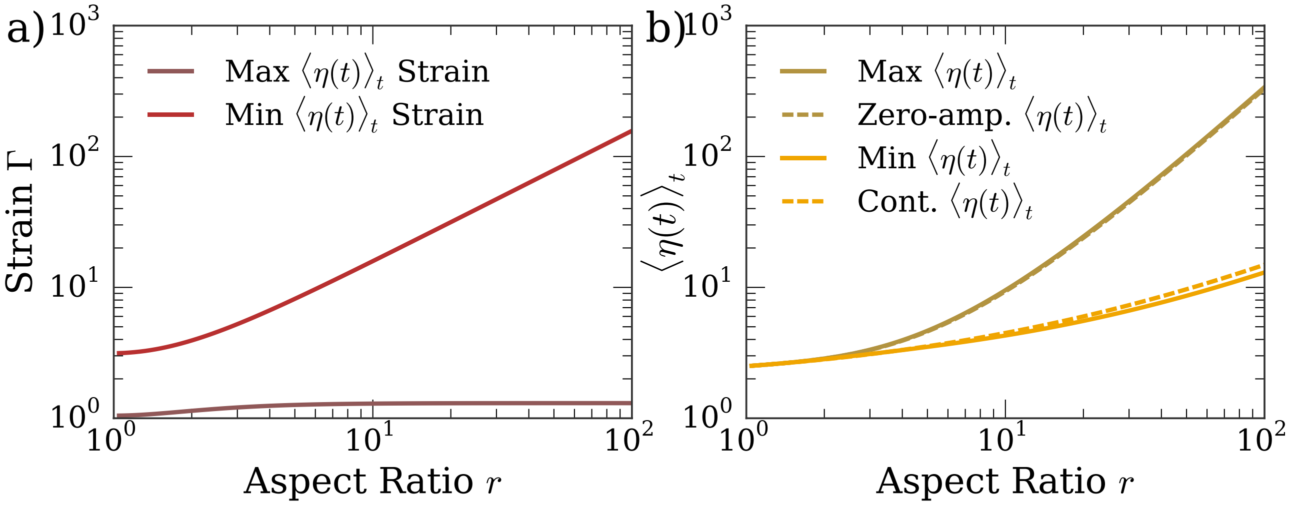

FIG. 6. (a) The scaling with aspect ratio of the strain that produces the maximal (brown) and minimal (red) $\langle\eta(t)\rangle_t$. (b) The scaling of the maximal (solid dark orange) and minimal (solid bright orange) $\langle\eta(t)\rangle_t$ with aspect ratio. The low-amplitude (dashed dark orange) and continuous shear (dashed bright orange) viscosities closely track these two curves.

does not change sign upon reversing time. While in principle a hydrodynamic normal stress difference can be nonzero at any instant of time, in practice hydrodynamic normal stress differences are usually prevented by additional symmetries. For instance, in simple shear reversing time corresponds to reflecting the flow axis. If the suspension microstructure is symmetric under this reflection, then the normal stress difference will be identically zero by symmetry. This symmetry prevents hydrodynamic normal stress differences from arising in suspensions of rods both at infinite Péclet [7] and at zero Péclet. As a result, most normal stresses in suspensions of nonspherical particles have a nonhydrodynamic origin, such as from Brownian motion or particle contacts [5,24,28,29,33,34].

While shear flows that vary simply in time usually produce no hydrodynamic normal stress differences, more complex waveforms can give rise to a nonzero first normal stress difference N1 strictly from hydrodynamics. In general, reversibility of Stokes flow requires that N1 time-average to 0. However, it is in principle possible to create complex waveforms that have a nonzero N1 at any instant of time during the oscillation. To understand the microstructural origins of a hydrodynamic N1, we look at the normal stress components σ_{xx} and σ_{yy} of Eq. (12), where the x is the flow direction and y the gradient. Substituting $\boldsymbol{p} = (n_x, n_y, 0)$ and evaluating the dot products shows that moments of the orientation distribution, weighted by AH, determine the hydrodynamic normal stress difference $N_1 = \sigma_{xx} - \sigma_{yy}$

$$N_1/\eta\dot{\gamma}c = \frac{1}{2}A_H\langle\sin 4\phi\rangle. \qquad (14)$$

There are also additional Brownian normal stresses in the suspension; however, since these stresses are $O(1/\mathrm{Pe})$ smaller than the hydrodynamic normal stresses, we ignore them in the analysis. As visible from Eq. (14), an orientation distribution that is symmetric $\phi \to -\phi$ always produces an identically zero hydrodynamic normal stress difference, which is why steady shear and low-amplitude oscillatory shear have $N_1 = 0$. For a general waveform, however, $\rho(\phi)$ does not have this symmetry, and a nonzero hydrodynamic N_1 is possible.

Measuring a nonzero hydrodynamic normal stress would have important consequences for rheological theories of rodlike particle suspensions. Frequently, normal stress differences are measured in steady shear at high Pe. These normal stress differences arise due to particle contacts, especially in the semidilute regime [34–37]. However, in a more dilute suspension this measured N_1 could arise either directly, from contacts, or indirectly, through the effect of particle contacts on the orientation distribution. Measuring the normal-stress coefficient A_H would provide insight into the range of normal stress differences that could be expected from hydrodynamics alone and further elucidate the origins of normal stress differences in suspensions of Brownian rods.

In light of this, we look for a waveform that optimizes the magnitude of the normal stress viscosity $A_H\langle\sin(4\phi)\rangle/2$ from Eq. (14) after the decay of initial transients ($Dt \gg 1$), imagining a measurement of this viscosity with a pump-probe experiment as for the shear viscosity. In contrast to the shear viscosities, due to reversibility of Stokes flow the average normal stress viscosity is always zero. Instead, we maximize the average of the absolute value of the normal-stress viscosity $|N_1/\eta c\dot{\gamma}|$, which will maximize the normal stress signal from a probe experiment at any given time. Moreover, maximizing the normal stress viscosity would facilitate a direct measurement of nonzero, hydrodynamic normal stress differences in a dilute suspension, as opposed to the usually nonhydrodynamic and semidilute regime normal stress differences that are currently measured [24,33–35,38].

Figure 7(a) displays the waveform that maximizes the signal from N_1 for a dilute suspension with $r = 5.0$. Like the waveforms that maximize and minimize the viscosity, the strain $\Gamma(t)$ takes a boxcar shape, alternating between a strain $\Gamma = 0$ and a moderate strain $\Gamma \approx 3.77$. This moderate strain produces a moderately peaked $f(\kappa)$, as shown in the upper portion of panel (b). The waveform aligns the peak of $f(\kappa)$ with one of the broad peaks in the normal-stress term $\sin(4\phi)/2$, before translating it to align $f(\kappa)$ with the nearby broad trough for the second half of the cycle. This produces a symmetric N_1 signal that averages to zero but has constant magnitude throughout the cycle, as shown in Fig. 7(c).

Examining Eq. (14) in detail divulges the structure of the optimal normal stress waveform. The normal stress term has four maxima corresponding to $\sin(4\phi) = 1$, at $\phi = (4n+1)\pi/8$, and four minima at $\phi = (4n-1)\pi/8$. The nonlinear $\phi \to \kappa$ transformation warps these equally spaced maxima in ϕ into the bunches of maxima and minima visible in Fig. 7(b). For instance, the close maximum/minimum pair near $\kappa = \pi$ are the image of the maximum at $\phi = 9\pi/8$ and the minimum at $\phi = 7\pi/8$. The Jeffery transformation in Eq. (1) places these two extrema at phase angles $\kappa + \varpi\Gamma = \pi \mp \tan^{-1}((\sqrt{2}-1)/r)$. Likewise, the broad outer extrema at $\kappa + \varpi\Gamma = \pi \mp \tan^{-1}((\sqrt{2}+1)/r)$ correspond to the maximum at $\phi = 5\pi/8$ and the minimum at $\phi = 11\pi/8$. This cluster of four extrema are separated from the other cluster near $\kappa + \varpi\Gamma = 0$ by a large, $\sim\pi$ distance.

One could try to maximize $|N_1|$ by aligning the peak of $f(\kappa)$ with either the inner set of extrema, at $\pi \pm \tan^{-1}((\sqrt{2}-1)/r)$, or the outer set of extrema, at $\pi \pm \tan^{-1}((\sqrt{2}+1)/r)$. However, for any waveform the peak of $f(\kappa)$ is at least of width $\sim 1/r$, as suggested in Eqs. (8) and (10). Thus, attempting to align $f(\kappa)$ with the inner maximum always results in significant overlap with the nearby inner minimum. To avoid this problem, the optimal waveform aligns the outer, broad extrema with the peak of $f(\kappa)$. The waveform first aligns $f(\kappa)$ with the broad maximum, producing a large, positive N_1. Aligning the broad maximum with $f(\kappa)$ reduces the overlap of $f(\kappa)$ with the nearby minimum and increases the normal stress signal. The waveform then reverses direction, aligning $f(\kappa)$ with the broad minimum to create a large, negative N_1.

In orientation space, the waveform alternates between aligning particles along the $5\pi/8$ and $11\pi/8$ axes, which are near the flow direction ($\phi = \pi/2$ or $3\pi/2$), as shown in Fig. 7(d). Positioning particles on these axes gives a large normal stress signal. The boxcar's strain amplitude is large enough to orient the distribution away from isotropy [Fig. 7(d)

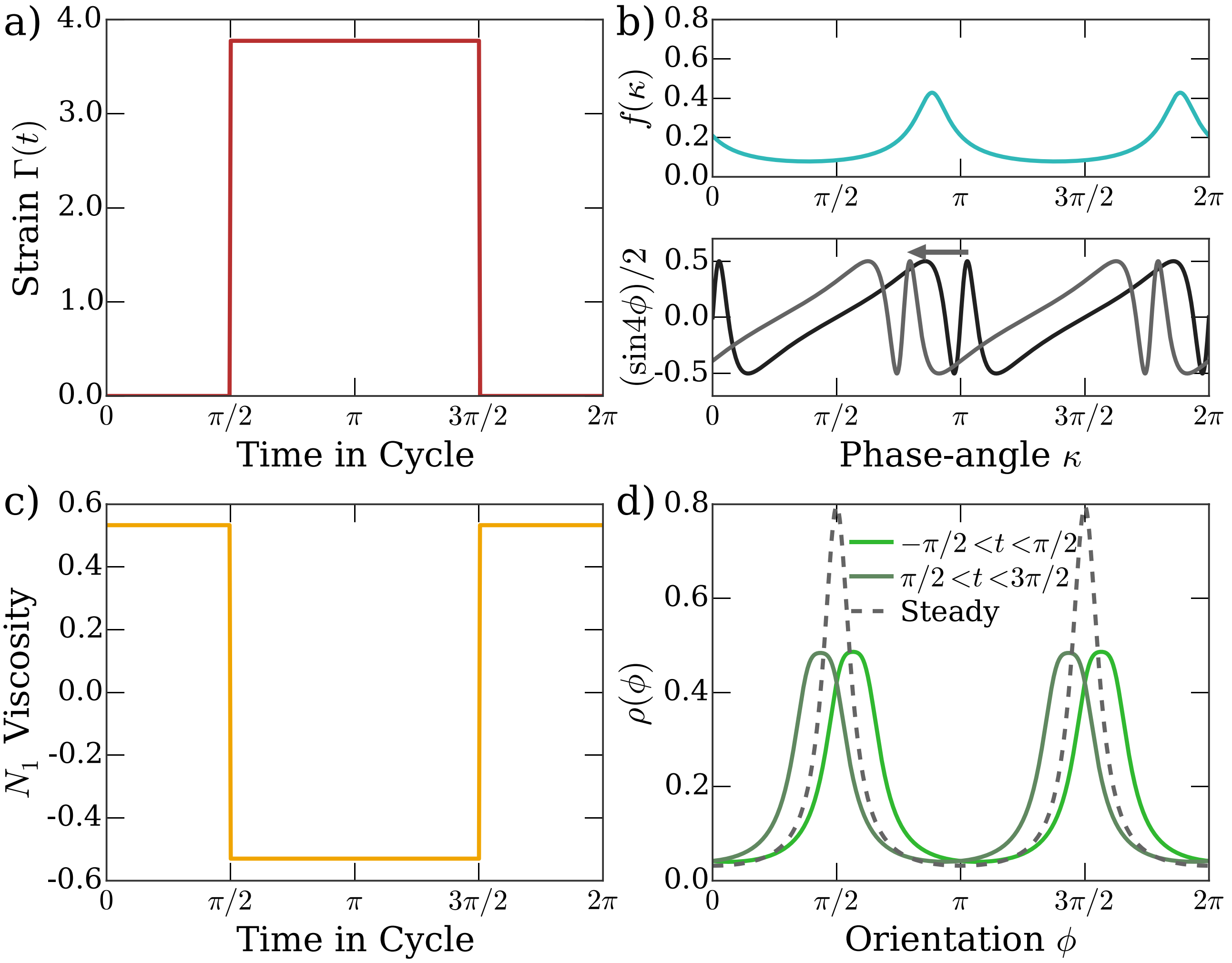

FIG. 7. (a) The waveform that maximizes the average of the absolute value of the normal-stress viscosity, for a suspension with $r = 5.0$. The optimal waveform has a ramp-width of zero, as shown in the figure. (b) Top panel: The corresponding $f(\kappa)$. Bottom panel: The corresponding normal stress term $\sin(4\phi)/2$ at the start of the cycle (black), and its position at the middle of the cycle (gray). (c) $N_1/\eta c\dot{\gamma}$ as a function of time in the cycle. $N_1/\eta c\dot{\gamma}$ is equal and opposite during the two halves of the cycle, averaging to zero. (d) The orientation distribution $\rho(\phi)$, for $-\pi/2 < t < \pi/2$ (light green) and for $\pi/2 < t < 3\pi/2$ (dark green), with the continuous shear distribution (dotted line) for comparison. Since the waveform is symmetric under time reversal, the two distributions are symmetric under a reflection about the gradient axis. The large normal stresses arise from orienting the particles along $\phi = (2n+1)\pi/8$, where the normal stress term is large in magnitude (multimedia view in the supplementary material).

(multimedia view in the supplementary material)]. In contrast, attempting to orient the particles onto the inner set of extrema, at $\phi = 7\pi/8$ and $9\pi/8$, results in a strain amplitude that is too small to significantly orient the distribution and that overlaps significantly with the adjacent extrema of opposite sign, creating a weak normal stress signal.

From this understanding of the optimal $|N_1|$ waveform, we can predict the scaling of the strain and normal stresses with aspect ratio. Since the broad maxima and minima are separated by $\delta\kappa = 2\tan^{-1}((\sqrt{2}+1)/r)$, and since $\bar{\omega} \sim 1/r$ for large r, alternating the alignment of $f(\kappa)$ between the two broad extrema should require a strain jump of $\Gamma \approx 2r\tan^{-1}((\sqrt{2}+1)/r) \approx 4.8$ for large r. Instead, Fig. 8(a) shows that Γ asymptotically approaches a strain of $\approx$5.22, which is slightly higher than the above value. By positioning the peak in $f(\kappa)$ slightly outside the skewed, broad extrema in the normal stress term, the optimal waveform reduces overlap with the nearby inner extrema of opposite sign. At moderate $r \lesssim 5$, the strain producing the maximal-$|N_1|$ approaches its asymptotic value slowly but still approximately follows the $\Gamma \sim 2r\tan^{-1}((\sqrt{2}+1)/r)$ scaling above. Like the case for the shear viscosity, $f(\kappa)$ for the normal stress waveform never approaches zero. As a result, the maximal and minimal values of the expectation $\langle\sin(4\phi)\rangle$ are always of order ± 1 independent of r, and the magnitude of the N_1 signal in Fig. 8(b) grows solely due to the growth of A_H with aspect ratio.

Interestingly, the magnitude of the normal stress created by the boxcar waveform scales differently than the normal stresses produced by fiber contacts. The boxcar waveform creates a large N_1 by strongly altering the orientation distribution from the steady shear distribution. As a result, the normal stress scales as $N_1/\dot{\gamma} \sim cA_H \sim cr^2/\ln r$, where c is the particle volume fraction. In contrast, interparticle contacts can only weakly affect the orientation distribution, since long aspect ratio particles rotate like lines of dye in the flow, and lines of dye do not intersect [35]. This weak change in the orientation distribution results in a normal stress that scales either as $N_1/\dot{\gamma} \sim cr$ [35] or as $N_1/\dot{\gamma} \sim cr^{3/2}$ [39], which increase more slowly with r than the boxcar's N_1. Thus, for large aspect ratio rods sheared with the optimal

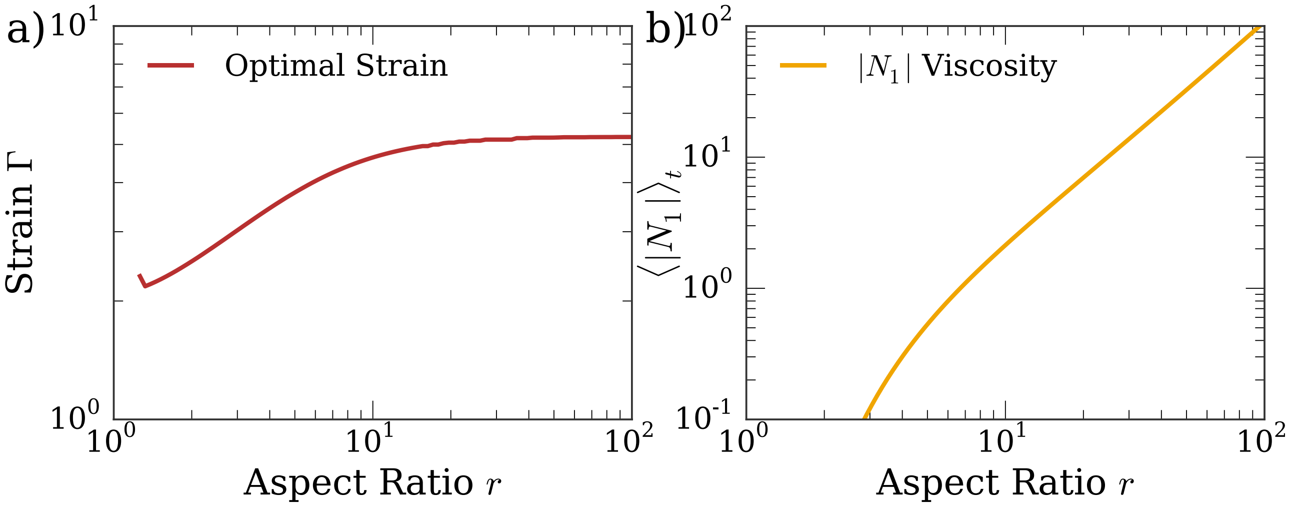

FIG. 8. The scaling with aspect ratio of (a) the boxcar waveform strain that produces the maximal normal stress signal, and (b) the normal stress viscosity itself.

boxcar waveform, the normal stress should be strictly hydrodynamic in origin with only weak corrections due to fiber contacts, and it should be possible to directly measure a hydrodynamic N_1 in a suspension of rodlike particles.

VI. CONCLUSIONS

In this paper, we have explored the possibility of designing oscillatory shear waveforms to control suspensions of rodlike particles, by examining the behavior of these suspensions at high $\mathrm{Pe} \equiv 1/DT_{cyc}$ and after initial transients have decayed ($Dt \gg 1$). Our approach to optimizing an oscillatory shear waveform is generic and can be implemented to optimize any desired property of a sheared suspension that depends on particle orientations. While an exhaustive exploration of waveforms for every property is impossible, many simple properties will be optimized by waveforms similar to those shown here. For instance, while particle alignment determines suspension conductivity [17] and flow-dichroism [40], the relevant order parameter is not the maximum of ρ but the liquid-crystal order parameter S_2, which is the maximal eigenvalue of the traceless symmetric second-rank orientation tensor $\boldsymbol{Q} = \boldsymbol{pp} - \boldsymbol{\delta}/2$. Likewise, the elasticity of a fiber-reinforced composite depends on fourth-order moments of the particle orientation, such as the analogous S_4. While these order parameters are different from the maximum of ρ, we find empirically that the waveform that maximizes ρ at the start of a cycle also maximizes S_2 and S_4. Alternatively, rather than maximize the particle alignment by maximizing $\rho(\phi)$, one might desire to minimize the particle alignment along one direction. We find empirically that the waveform in Fig. 2 that maximizes particle alignment also most strongly minimizes the particle alignment along a different direction—the strong enhancement of $\rho(\phi) \sim r^2$ at $\phi = \pi/2,\ 3\pi/2$ also results in a $\sim 1/r^2$ suppression of orientations at $\phi = 0,\ \pi$.

All of our analysis has necessarily been limited to orientations confined to rotate in the flow-gradient plane, as there is no simple solution for fully rotating particle orientations under arbitrary shear waveforms. Nevertheless, while the quantitative details of the results may change for fully three-dimensional orientations, the qualitative picture should remain the same. The ϕ dynamics of a freely rotating particle in a simple shear flow are the same as one confined to the flow-gradient plane. Moreover, preliminary analysis [9] and experiments [10] suggests that the κ dynamics remain similar for freely rotating orientations as for those confined to the flow-gradient plane. Since the results above have simple interpretations in terms of the particle phase angles κ, the optimal waveforms should be similar for real suspensions.

The waveform that maximizes particle alignment should remain the same for freely rotating particles. The simplicity of the spike waveform allows for the calculation of the orientation distribution for freely rotating particle orientations. For almost all of the spike waveform, the particle orientations are at rest at a single strain value. Keeping the orientations at rest causes diffusion to drive the distribution to isotropy for most of the cycle, as for the orientations confined to the flow-gradient plane considered above. The spike then advects this initially isotropic distribution by one-quarter of a Jeffery orbit, rapidly enough where diffusion cannot alter the distribution. Thus, the distribution at the center of the spike is the same as that of an isotropic distribution advected by one-quarter of a Jeffery orbit without diffusion, which is easily calculable analytically [41]

$$\rho(\theta,\phi) = \frac{1}{4\pi}\frac{1}{\left[\cos^2\theta + \left(r^2\cos^2\phi + r^{-2}\sin^2\phi\right)\sin^2\theta\right]^{3/2}}. \tag{15}$$

The distribution is maximal along the flow direction, at $\theta = \pi/2$ and $\phi = \pi/2$, with a value $\rho(\pi/2, \pi/2) \propto r^3$. The spike aligns both the particle's azimuthal angle ϕ and polar angle θ. As visible from Eq. (1), the Jeffery orbits pinch near the flow direction, with the separation between particles on different orbits decreasing by an amount $\sim 1/r$ when oriented along the flow direction versus along the gradient direction. Since the spike waveform first orients a large fraction of

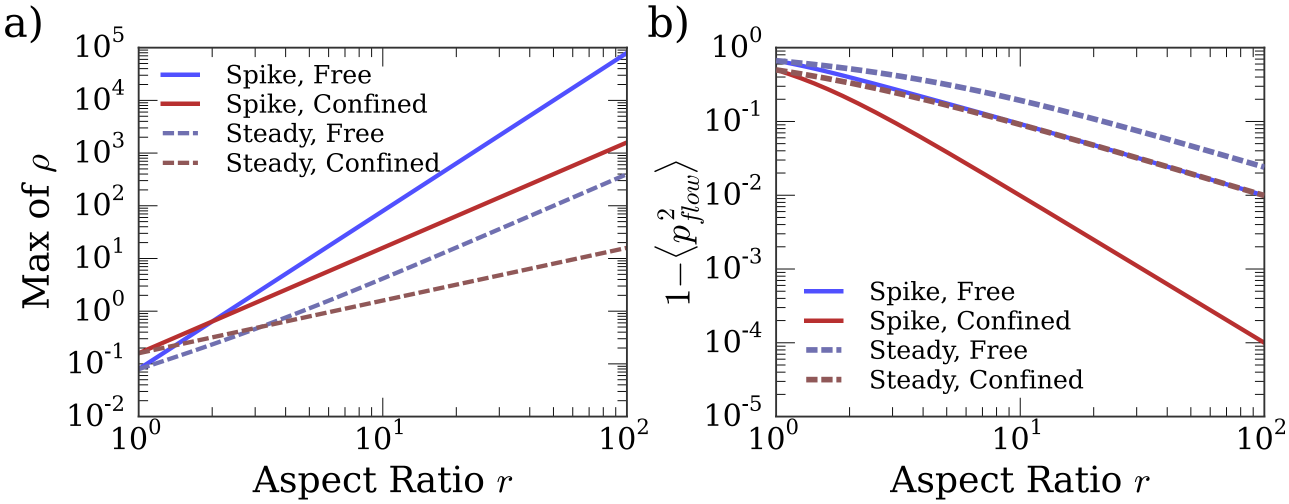

FIG. 9. Orientation alignment for freely rotating orientations. (a) Alignment as measured by the maximal value of $\rho(\phi)$, for both freely rotating orientations (blue) and orientations confined to the flow-gradient plane (red), under both the optimally aligning spike waveform (solid lines) and steady shear (dashed lines). (b) Alignment as measured by $1-\langle p^2_{flow}\rangle$, where p_{flow} is the projection of the rod's unit normal along the flow direction.

particles near the gradient direction before rapidly rotating them to the vorticity direction, it strongly pinches the distribution into a $\sim 1/r$ region in θ. Moreover, since the phase angle κ completely determines the azimuthal angle ϕ, the spike waveform in Sec. III will still align the ϕ component of the particle orientations into a $\sim 1/r^2$ region. Combining these two effects results in the $\sim r^3$ alignment visible in Eq. (15). Due to the additional spread in θ, freely rotating orientations are less strongly aligned than orientations confined to the flow gradient plane, as shown by the plot of $1-\langle p^2_{flow}\rangle$ shown in Fig. 9. Nevertheless, since the spike waveform takes advantage of both the $\sim 1/r$ pinching of the orbits and their $\sim 1/r^2$ bunching, it aligns particle orientations more strongly than continuous shear, and we expect that the spike waveform optimally aligns real, freely rotating particle orientations.

The waveforms that extremize the viscosity should also be similar between freely rotating orientations and those confined to the flow-gradient plane. Two separate effects change the rheology of a suspension of freely rotating particles. First, the rocking of the Jeffery orbit changes the θ component of the orientation, creating an additional source of time dependence in the orientation moments that determine the suspension stress. Second, the form of the orientation moments themselves changes when the particle orientations have a nonzero component along the vorticity direction. For example, the variations in the shear stress are completely determined by the moment $A_H\langle 1-\cos 4\phi\rangle/8$ when the particle orientations are confined to the flow-gradient plane, cf. Eqs. (12) and (13). Moreover, when the particles rotate freely, an additional orientation-dependent moment $B_H\langle n_x^2 + n_y^2\rangle$ also enters into the shear stress. This additional moment oscillates in magnitude with strain as the Jeffery orbit rocks particle orientations toward and away from the vorticity direction. However, the magnitude of B_H decreases rapidly as the particle aspect ratio increases, while that of A_H increases significantly [4]. As a result, the waveforms that extremize the shear viscosity for real suspensions should only differ slightly from those with orientations confined to the flow-gradient plane, with the differences solely due to the rocking of orientations toward and away from the vorticity direction. The waveform that extremizes the normal stress viscosity should likewise remain similar to that discussed above, as the moment that determines N_1 changes only slightly from that in equation (14) to $A_H\langle \sin^4\theta \sin 4\phi\rangle/2$, only picking up a factor of $\sin^4\theta$.

Possessing a full solution to the orientation dynamics would allow for investigation of these properties. More interestingly, a full solution would allow for the possibility of controlling shear flows where the principle axes of the strain change directions during the course of a cycle. Such waveforms could perhaps separately maximize the signal from all the hydrodynamic coefficients A_H, B_H, and C_H.

ACKNOWLEDGMENTS

The authors would like to thank S. Whitehead and L. Bartell for useful discussions. I.C. and B.L. were supported by the National Science Foundation (NSF) CBET-PMP Award No. 1232666 and continued support from NSF CBET-PMP Award No. 1509308. D.L.K was supported by the National Science Foundation (NSF) Grant No. CBET-PMP-1435013.

APPENDIX: NUMERICAL METHODS

1. Numerical methods

To find the optimal waveforms, we parameterized the distributions by the lowest 80 real Fourier coefficients. For all of the properties optimized in the text, there are many local minima in this fit space of Fourier coefficients. For instance, frequency-doubling a waveform produces the same distribution as the original waveform, aside from differences due to a finite number of Fourier coefficients. Reversing time $\Gamma(t)\rightarrow\Gamma(-t)$ or the sign $\Gamma(t)\rightarrow-\Gamma(t)$ do not change the distributions. Shifting a waveform by a half-integer Jeffery orbit $\Gamma(t)\rightarrow\Gamma(t)+n\pi(r+1/r)/2$ does not change the distributions. For the properties that are averages over a cycle, shifting the phase of the waveform $\Gamma(t) \rightarrow \Gamma(t+\delta)$ does not change the measured response. Combining these transformations creates a complicated fit landscape with many local minima and equivalent waveforms. To navigate this landscape, we chose 100 random initial guesses for the Fourier coefficients and optimized each one of these with a deterministic BFGS algorithm as implemented in PYTHON (scipy) [42]. We chose BFGS because it assumes that a minimum is locally quadratic in the fit parameters, which is the case for our parameterization.

The results of these 100 fits for each waveform are shown in Fig. 10, with the top 5 of the 100 waveforms highlighted. The plot clearly demonstrates the complexity of the fit landscape. For instance, the maximal alignment waveforms [panel (a)] show a jump between equivalent waveforms separated by half a Jeffery orbit in strain. Phase shifts, sign changes, and period doubling are clearly visible in the extremal viscosity and normal stress waveforms. In addition, since the optimal waveforms are not smooth, significant Gibbs ringing is visible in the fitted waveforms. Fortunately, since the waveform determines the long-time phase angle distribution $f(\kappa)$ through an integral relation [Eq. (7)], the short Gibbs ringing deviations from the optimal waveform have little effect on $f(\kappa)$.

Examining the best waveforms by eye quickly divulges what the correct simple, optimal waveform should be (e.g., the spike and boxcar waveforms); the vast majority of the fitted waveforms have a variation on the boxcar or spike waveform. Using the realization that the optimal waveforms are simpler spikes or boxcars, we then reoptimize using the simpler waveform with several free parameters. For the spike waveform, we optimize the spike height, ramp time, and phase, and for the boxcar the boxcar height, boxcar width, and ramp time—since the optimized viscosities are averages over the waveform, we do not optimize the boxcar phase. For the optimal distributions as well as the shear and normal stresses, the simple waveforms always produce a better value than any of the Fourier-parameterized waveforms, probably due to the slow convergence of the Fourier basis due to Gibbs ringing. Finally, to evaluate the scalings with aspect ratio we only optimized over the simple waveform, at 100 aspect ratios logarithmically spaced from 1 to 100. This approach of starting with a model-independent Fourier

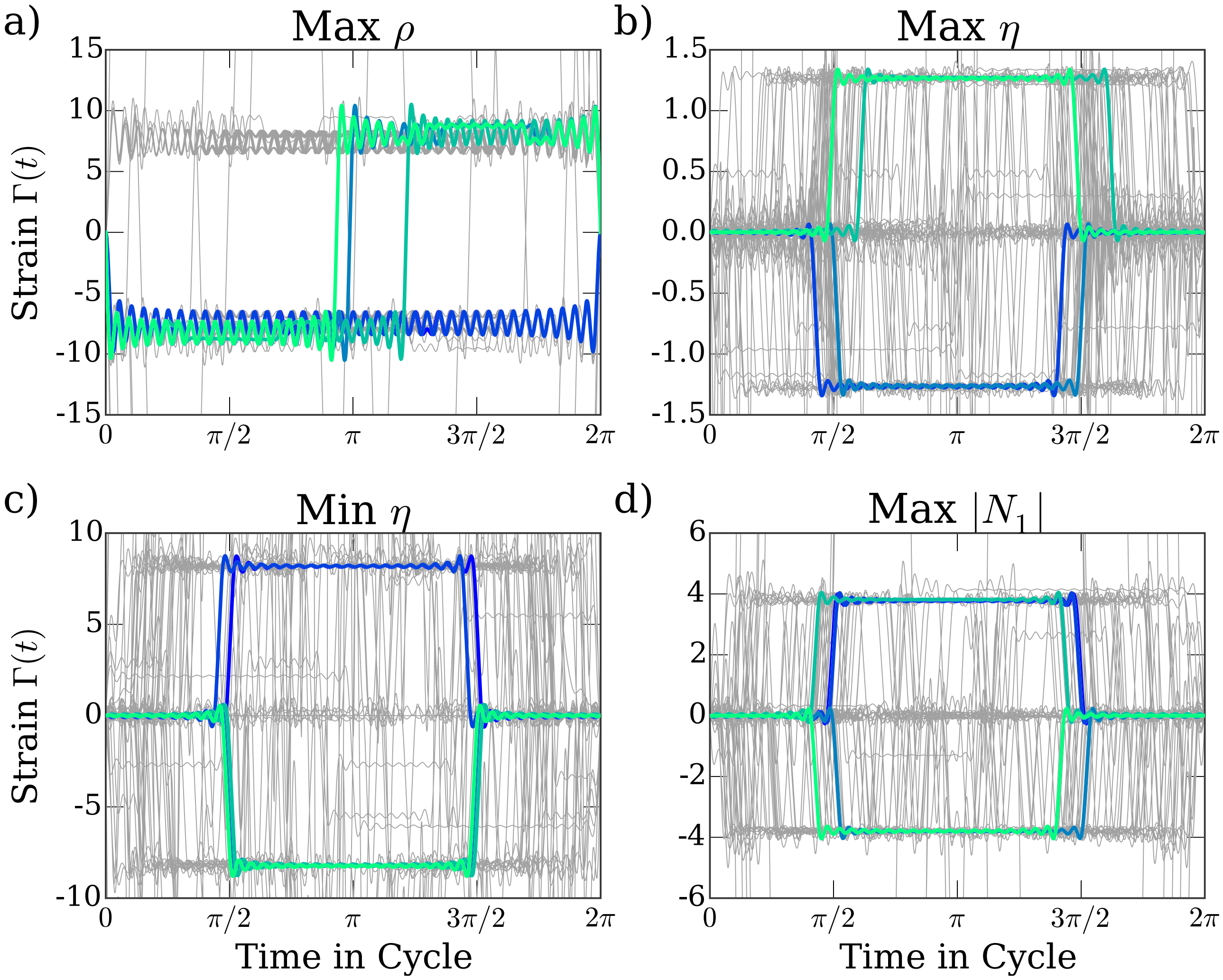

FIG. 10. All 100 of the best-fit Fourier waveforms for maximizing alignment (a), maximizing viscosity (b), minimizing viscosity (c), and maximizing normal stress signals (d). The 5 best waveforms for each case are highlighted, with the best waveform in green and the fifth-best in blue; the other 95 are in gray. With the exception of the maximal alignment Fourier waveforms, the highlighted waveforms for each panel produce an equal response to 1 part in 10^4.

search and finishing with a parameterized model of the optimal waveform provides the best of both worlds, promising the optimal waveform through the breadth of the Fourier search and the providing the best-possible value through a waveform that eliminates Gibbs ringing.

To evaluate distributions and stresses for a particular waveform, we evaluated the coefficients A_2, δ_2, A_4, δ_4 from Eq. (10) numerically and used those coefficients to reconstruct $\mathfrak{D}(\kappa)$ and a numerically normalized $f(\kappa)$. Empirically, it is necessary to use a somewhat high number of quadrature points (900 for $r = 5.0$ and up to 12 000 for the $r = 100.0$ values shown in the scaling plots), as the waveforms discussed in this paper are somewhat pathological and not analytic, and a simple trapezoidal rule is therefore not exponentially convergent [42]. For the tent and spike waveforms, we choose the quadrature points to be only where the waveform is varying, while for the Fourier waveforms we used equally spaced quadrature points.

References

[1] Jeffery, G. B., "The motion of ellipsoidal particles immersed in a viscous fluid," Proc. R. Soc. Lond. A **102**, 161–179 (1922).

[2] Singh, V., D. L. Koch, and A. D. Stroock, "Rigid ring-shaped particles that align in simple shear flow," J. Fluid Mech. **722**, 121–158 (2013).

[3] Bretherton, F. P., "The motion of rigid particles in a shear flow at low Reynolds number," J. Fluid Mech. **14**, 284–304 (1962).

[4] Kim, S., and S. Karrila, *Microhydrodynamics: Principles and Selected Applications* (Dover Publications, Mineola, NY, 2005).

[5] Mewis, J., and N. J. Wagner, *Colloidal Suspension Rheology* (Cambridge University, Cambridge, UK, 2012).

[6] Leal, L. G., and E. J. Hinch, "The effect of weak Brownian rotations on particles in shear flow," J. Fluid Mech. **46**, 685–703 (1971).

[7] Hinch, E. J., and L. G. Leal, "The effect of Brownian motion on the rheological properties of a suspension of non-spherical particles," J. Fluid Mech. **52**, 683–712 (1972).

[8] Hinch, E. J., and L. G. Leal, "Time-dependent shear flows of a suspension of particles with weak Brownian rotations," J. Fluid Mech. **57**, 753–767 (1973).

[9] Leahy, B. D., D. L. Koch, and I. Cohen, "The effect of shear flow on the rotational diffusion of a single axisymmetric particle," J. Fluid Mech. **772**, 42–79 (2015).

[10] Leahy, B., X. Cheng, D. C. Ong, C. Liddell-Watson, and I. Cohen, "Enhancing rotational diffusion using oscillatory shear," Phys. Rev. Lett. **110**, 228301 (2013).

[11] Hinch, E. J., *Perturbation Methods* (Cambridge University, Cambridge, UK, 1991).

[12] Reeks, M. W., "The transport of discrete particles in inhomogeneous turbulence," J. Aerosol. Sci. **14**, 729–739 (1983).

[13] Balkovsky, E., G. Falkovich, and A. Fouxon, "Intermittent distribution of inertial particles in turbulent flows," Phys. Rev. Lett. **86**, 2790–2793 (2001).

[14] Corté, L., P. M. Chaikin, J. P. Gollub, and D. J. Pine, "Random organization in periodically driven systems," Nat. Phys. **4**, 420–424 (2008).

[15] Franceschini, A., E. Filippidi, E. Guazzelli, and D. J. Pine, "Transverse alignment of fibers in a periodically sheared suspension: An absorbing phase transition with a slowly varying control parameter," Phys. Rev. Lett. **107**, 250603 (2011).

[16] Fu, S.-Y., and B. Lauke, "The elastic modulus of misaligned short-fiber-reinforced polymers," Compos. Sci. Technol. **58**, 389–400 (1998).

[17] Rocha, A., and A. Acrivos, "On the effective thermal conductivity of dilute dispersions general theory for inclusions of arbitrary shape," Quart. J. Mech. Appl. Math. **26**, 217–233 (1973).

[18] Shaqfeh, E. S. G., "A nonlocal theory for the heat transport in composites containing highly conducting fibrous inclusions," Phys. Fluids (1958–1988) **31**, 2405–2425 (1988).

[19] Sundararajakumar, R. R., and D. L. Koch, "Electrical conductivity of isotropic fibre suspensions," Proc. R. Soc. London A: Math. Phys. Eng. Sci. **455**, 1923–1930 (1999).

[20] Frattini, P. L., and G. G. Fuller, "The dynamics of dilute colloidal suspensions subject to time-dependent flow fields by conservative dichroism," J. Colloid Interface Sci. **100**, 506–518 (1984).

[21] See supplementary material at http://dx.doi.org/10.1122/1.4996009 for movies of the optical distributions during an oscillatory cycle.

[22] Brenner, H., "Rheology of a dilute suspension of axisymmetric Brownian particles," Int. J. Multiphase Flow **1**, 195–341 (1974).

[23] Peterlin, A., "Über die viskosität von verdünnten lösungen und suspensionen in abhängigkeit von der teilchenform," Z. Phys. **111**, 232–263 (1938).

[24] Sepehr, M., P. J. Carreau, M. Moan, and G. Ausias, "Rheological properties of short fiber model suspensions," J. Rheol. (1978-present) **48**, 1023–1048 (2004).

[25] Chaouche, M., and D. L. Koch, "Rheology of non-Brownian rigid fiber suspensions with adhesive contacts," J. Rheol. **45**, 369–382 (2001).

[26] Letwimolnun, W., B. Vergnes, G. Ausias, and P. J. Carreau, "Stress overshoots of organoclay nanocomposites in transient shear flow," J. Non-Newtonian Fluid Mech. **141**, 167–179 (2007).

[27] Eberle, A., G. M. Vélez García, D. G. Baird, and P. Wapperom, "Fiber orientation kinetics of a concentrated short glass fiber suspension in startup of simple shear flow," J. Non-Newtonian Fluid Mech. **165**, 110–119 (2010).

[28] Khair, A. S., "On a suspension of nearly spherical colloidal particles under large-amplitude oscillatory shear flow," J. Fluid Mech. **791**, R5 (2016).

[29] Leal, L. G., and E. J. Hinch, "The rheology of a suspension of nearly spherical particles subject to Brownian rotations," J. Fluid Mech. **55**, 745–765 (1972).

[30] Strand, S. S., S. Kim, and S. J. Karrila, "Computation of rheological properties of suspensions of rigid rods: Stress growth after inception of steady shear flow," J. Non-Newtonian Fluid Mech. **24**, 311–329 (1987).

[31] Chen, L.-Y., N. Goldenfeld, and Y. Oono, "Renormalization group and singular perturbations: Multiple scales, boundary layers, and reductive perturbation theory," Phys. Rev. E **54**, 376–394 (1996).

[32] Batchelor, G. K., "The stress system in a suspension of force-free particles," J. Fluid Mech. **41**, 545–570 (1970).

[33] Petrich, M., C. Cohen, and D. L. Koch, "An experimental determination of the stress-microstructure relationship in semi-concentrated fiber suspensions," J. Non-Newtonian Fluid Mech. **95**, 101–133 (2000).

[34] Snook, B., L. M. Davidson, J. E. Butler, O. Pouliquen, and E. Guazzelli, "Normal stress differences in suspensions of rigid fibres," J. Fluid Mech. **758**, 486–507 (2014).

[35] Sundararajakumar, R. R., and D. L. Koch, "Structure and properties of sheared fiber suspensions with mechanical contacts," J. Non-Newtonian Fluid Mech. **73**, 205–239 (1997).

[36] Eberle, A. P. R., D. G. Baird, P. Wapperom, and G. M. Vélez-García, "Obtaining reliable transient rheological data on concentrated short fiber suspensions using a rotational rheometer," J. Rheol. (1978-present) **53**, 1049–1068 (2009).

[37] Férec, J., G. Ausias, M. C. Heuzey, and P. J. Carreau, "Modeling fiber interactions in semiconcentrated fiber suspensions," J. Rheol. (1978-present) **53**, 49–72 (2009).

[38] Keshtkar, M., M. C. Heuzey, and P. J. Carreau, "Rheological behavior of fiber-filled model suspensions: Effect of fiber flexibility," J. Rheol. (1978–present) **53**, 631–650 (2009).

[39] Zirnsak, M. A., D. U. Hur, and D. V. Boger, "Normal stresses in fibre suspensions," J. Non-Newtonian Fluid Mech. **54**, 153–193 (1994).

[40] Frattini, P. L., and G. G. Fuller, "Rheo-optical studies of the effect of weak Brownian rotations in sheared suspensions," J. Fluid Mech. **168**, 119–150 (1986).

[41] Okagawa, A., R. G. Cox, and S. G. Mason, "The kinetics of flowing dispersions vi: Transient orientation and rheological phenomena of rods and discs in shear flow," J. Colloid Interface Sci. **45**, 303–329 (1973).

[42] Press, W. H., *Numerical Recipes: The art of scientific computing*, 3rd ed. (Cambridge University, Cambridge, UK, 2007).